BMC Chemistry

RESEARCH

Open Access

Design, synthesis, biological assessments and computational studies of 3-substituted phenyl quinazolinone derivatives as promising anti-cancer agents

Maryam Moghtader Mansouri[1], Leila Emami[2], Zahra Rezaei[1] and Soghra Khabnadideh[1,2*]

Abstract

A new series of 3-substituted phenyl quinazolinone derivatives were designed and synthesized as anti-cancer agents. The most potent derivative with IC_{50} values of 12.84 ± 0.84 and 10.90 ± 0.84 µM against MCF-7 and SW480 cell lines was comparable to Cisplatin and Erlotinib as positive controls. Cell cycle analysis showed that the most active compound could arrest at S phase in MCF-7 breast cancer cells. The apoptosis assay demonstrated the induction of apoptosis in the MCF-7 cell line, too. Molecular docking results showed better accommodation of the most active compound through hydrogen bonding interaction in the binding site of EGFR enzyme. Molecular dynamics simulations for the potent analogue demonstrated well binding stability compared to the less active analogue, with a lower RMSD, Rg and more interactions with the original active site residues. DFT calculations were performed on the active and inactive compounds, using Gaussian 09 at the M06-2X/6–31 + G(d) theoretical level. ADME (Absorption, Distribution, Metabolism, and Excretion) properties showed that most of the compounds are in acceptable range of Lipiniski rule. These findings underscore the potential of the synthesized compounds as potent cytotoxic inhibitors and provide insights for developing effective treatments for cancer therapy.

Keywords Quinazoline, Hydrazine, MTT, Cell cycle, Apoptosis, Molecular dynamic simulation

Introduction

Cancer continues to be a significant global health issue, marked by substantial rates of illness and death. The World Health Organization (WHO) identifies cancer as the second leading cause of death worldwide, with around 9.6 million deaths recorded in 2018. Projections indicate a notable rise in new cancer cases, anticipated to grow from 14.1 million in 2012 to approximately 21.6 million by the year 2030 [1–4].

Currently, cancer treatment includes standard interventions such as chemotherapy, surgery, and radiotherapy. Although these strategies can achieve initial successes, they often lack specificity, which may result in unintentional damage to surrounding healthy tissues and a range of adverse effects [5, 6]. This has led to the development of targeted therapies designed to take advantage of the distinct molecular features present in cancer cells. The approach of molecular targeting focuses on key enzymes or receptors associated with cancer, improving the precision of tumor treatment while minimizing adverse effects [7–10]. A significant focus in targeted cancer therapies involves inhibiting receptor

*Correspondence:
Soghra Khabnadideh
khabns@sums.ac.ir
[1] Department of Medicinal Chemistry, Faculty of Pharmacy, Shiraz University of Medical Sciences, Shiraz, Iran
[2] Pharmaceutical Sciences Research Center, Faculty of Pharmacy, Shiraz University of Medical Sciences, Shiraz, Iran

protein tyrosine kinases (RTKs), especially those that play a role in signaling pathways related to growth factors that promote tumor development and progression [11–15].

The epidermal growth factor receptor (EGFR) is a key component of the ErbB family of receptors, which regulate essential cellular functions like cell growth, development, and survival. It is a tyrosine kinase cell surface receptor that plays a key function in signal transduction processes and is found on most cell surfaces [16]. In various type of cancers, such as breast, lung, and colorectal cancers, as well as head and neck squamous cell carcinoma, EGFR is frequently overexpressed or mutated, leading to abnormal signaling pathways that drive tumor growth and spread [17, 18]. This has highlighted EGFR as an important target for cancer therapies. As a result, the creation of small molecules that specifically target EGFR has become a widely recognized strategy in the development of antitumor agents [19–22].

Nitrogen heterocycles constitute the pharmacophore moieties of various molecules with different biological activities, including antitumor activity due to their ability to bind with target proteins [23–25]. According to numerous researches, quinazoline derivatives have demonstrated significant antitumor activity as selective and potent EGFR inhibitors. Erlotinib and Gefitinib as first generation of EGFR inhibitors and Canertinib, Dacomitinib, and Afatinib as second generation of EGFR inhibitors have been developed for the treatment of cancers with EGFR overexpression [1, 26–32]. These drugs highlight the potential of quinazoline derivatives as a promising scaffold for the development of EGFR inhibitors. Despite the therapeutic successes of these approved drugs, resistance and side effects highlight the need for further research on this class of compounds to find drugs with fewer side effects [12, 33] (Fig. 1).

Following our previous studies on EGFR inhibitors as antitumor agents [34], in this study, we have designed, synthesized, and characterized a series of novel quinazoline derivatives by adding alternative groups at different positions of the quinazoline ring. The synthesized compounds were evaluated for their cytotoxicity, as well as their effects on the cancer cell cycle and their capacity to induce apoptosis. Furthermore, molecular docking study and molecular dynamics (MD) simulation were conducted to investigate the possible mechanisms of action for this class of compounds.

Results and discussion

Rational design

The epidermal growth factor receptor (EGFR) comprises of two domains: an extracellular receptor domain linked by a transmembrane region to an intracellular domain that possesses tyrosine kinase activity [35]. Using of tyrosine kinase inhibitors (TKIs) for inhibition of EGFR can delay downstream signaling effects and inhibit tumor growth. These inhibitors act by competitive blocking the binding of adenosine triphosphate (ATP) in the tyrosine kinase domain [36]. The overexpression or mutation of EGFR in various cancers, such as breast, lung, and colorectal cancers,

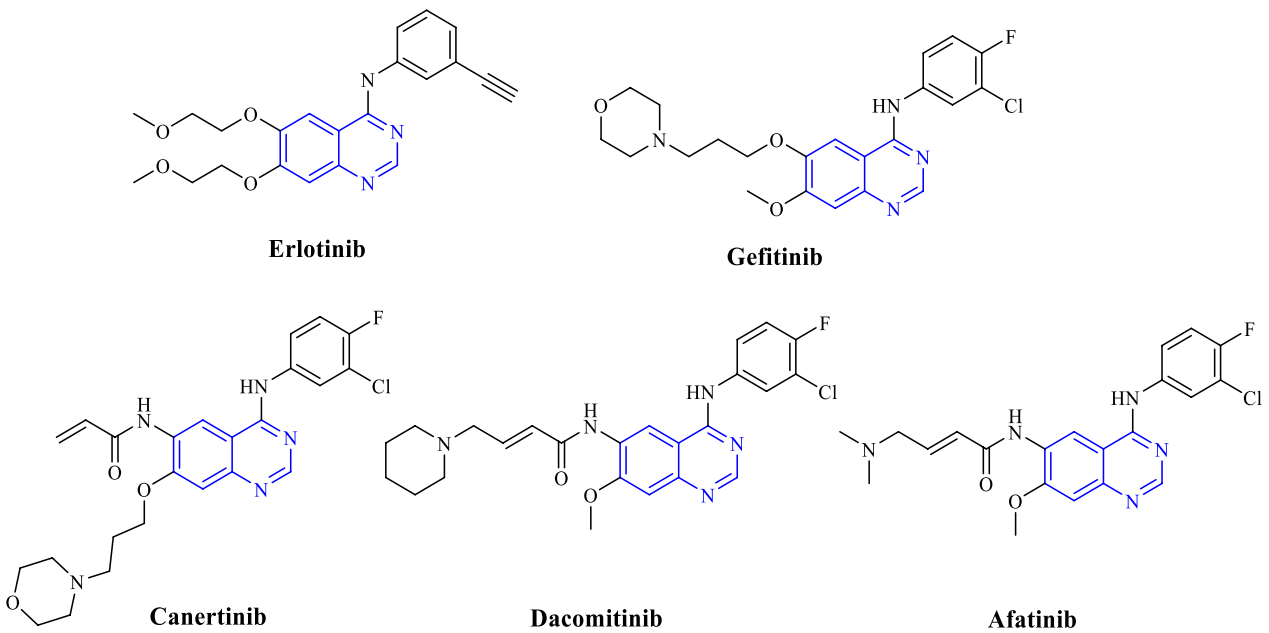

Fig. 1 The chemical structures of some EGFR inhibitors with quinazoline scaffold as anticancer agents

has been confirmed. Therefore, EGFR is an attractive target for anticancer therapy, and a large number of EGFR tyrosine kinase inhibitors have been developed [11, 17, 37, 38].

Numerous studies have emphasized the crucial role of quinazoline derivatives as selective and potent inhibitors of EGFR, along with their significant antitumor activity [1, 27, 28]. Among the promising candidates, quinazoline-4-one derivatives represent a novel pharmacophoric scaffold capable of potently inhibiting EGFR activity [26, 39–42]. Given the importance of the quinazoline scaffold, it was incorporated into the structure of the designed compounds, which bind to the ATP binding pocket of EGFR. Furthermore, bulky substituents at the N-3 position of the quinazoline ring were expected to target the hinge binding region, thereby providing a more stable and favorable positioning. It has been found that the halogens (Cl and Br) on the quinazoline ring leads to an increased in antitumor activity [26, 43]. Introduction of various groups, such as hydrazine, hydrazine derivative, and urea derivatives with varied hydrophilic and lipophilic characteristics, at C-2 position of the quinazoline ring was performed to investigate the potential of these moieties for EGFR inhibition (Fig. 2).

Virtual screening and molecular docking results

A diverse virtual library of 106 compounds was generated by introducing substituents (e.g., electron-donating/withdrawing groups, halogens, alkyl chains) to the quinazoline core and phenyl ring. Substituent selection aimed to modulate electronic, steric, and hydrophobic properties while maintaining synthetic feasibility. In this situation, Compounds were ranked by binding energy, with 15 derivatives selected by (Binding Energy ≥ -8.2 kcal/mol).

Docking model study was used to elucidate the mode and orientation of all the synthesized compounds in the active site of EGFR. To evaluate the docking protocol, redocking operation was done. As shown in Fig. 3, the RMSD value between the internal ligand (Erlotinib) before and after the docking is lower than 2Å that validated the docking procedure and RMSD of docking was found to be 1.23 Å. The score binding and interaction details of all designed compounds (**7a**–**7o**) and Erlotinib as internal ligand was shown in Table 1.

The interaction of the most potent (**7k** and **7j**) and the least potent compounds (**7a** and **7e**) were exhibited in Fig. 4. The rest interaction diagram of compounds was presented in supplementary file (Figure S46-S56). In the docked model, **7k** and **7j** represented desirable binding

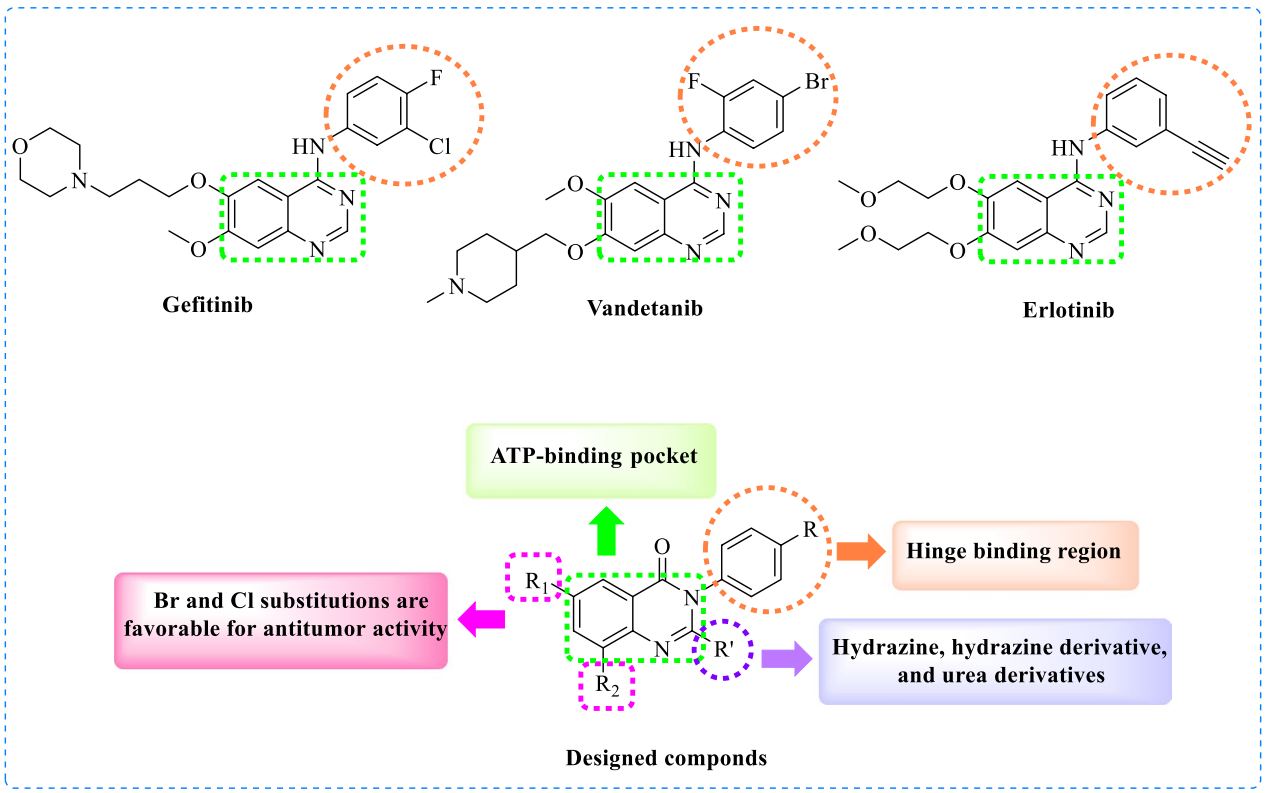

Fig. 2 Design of the target compounds **7a**–**7o**

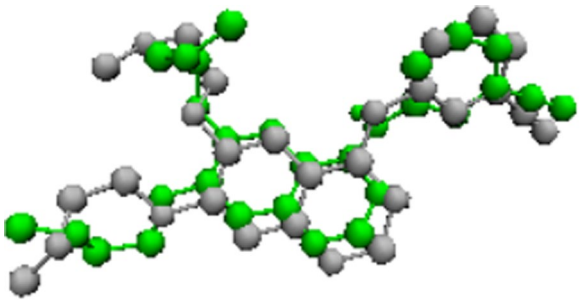

Fig. 3 The superimposing of the internal ligand (Erlotinib) before and after the docking operation was displayed (RMSD = 1.23 Å)

affinity within EGFR enzyme. In the both compounds, the hydrazine moiety forming hydrogen bonds with Asp 831 and Thr 830 in the ATP-binding site of the receptor. The substituted phenyl moiety interacted in pi-pi and pi-Anion interaction with Phe 699 and Asp 831 residues and the three CH-pi interactions between Leu 820, Leu 694, Val 702 residues and the quinazoline ring was observed. Also, EGFR involved various part of quinazoline motif by three hydrophobic interactions with Leu 820, Leu 694 and Val 702 residues. This significant binding interaction could be responsible for cytotoxic inhibition potency of **7k** and **7j** toward EGFR target**.** It is noteworthy that these compounds occupy the binding site of EGFR target.

On the other hand, amino acid residues Lys 721, Thr 766, Gln 767, Leu 768 and Gly 695 have formed hydrophobic interaction with analogue **7a**. Some other interactions like pi-sigma, pi-pi, pi-anion and CH-pi bonding were seen with Val 702, Phe 699, Asp 831, Ala 719, Leu 820, Leu 694 and Met 769. Likewise, EGFR tyrosine kinase receptor interacted with **7e** via pi-anion, pi-pi, pi-sigma, CH-pi and hydrophobic interaction with Asp 831, Phe 699, Leu 694, Val 702, Leu 820, Leu 768, Met 769, Ala 719, Gly 772, Pro 770, Gln 767, Thr 830, Lys 721 and Glu 738.

Chemistry

A novel series of quinazolinone derivatives was synthesized via a three-step process, as illustrated in Fig. 5. The initial step involved a nucleophilic substitution reaction between anthranilic acid derivatives (**1**) (or 2-aminobenzoic acid derivatives) and phenyl isothiocyanate derivatives. This reaction was carried out in the presence of triethylamine as a base and ethanol as a solvent at 70 °C for 24 h, resulting in the formation of compound **3**. Subsequently, compound **3** (2-mercapto-3-phenylquinazolin-4(3H)-one) was subjected to a reaction with methyl iodide (**4**) in dimethylformamide (DMF) under basic conditions using potassium carbonate. After 4 h, 2-methylthio-3-phenylquinazolin-4(3H)-one was obtained in high yield. In the final step, the synthesized 2-methylthio-3-phenylquinazolin-4(3H)-one derivatives (**5**) were reacted with hydrazine hydrate and urea derivatives (**6**) in DMF using potassium carbonate as a catalyst for 20 h, affording the final products (**7**) in excellent yields.

In the FT-IR spectra of the synthesized compounds (**7a**–**7o**), characteristic absorption bands for O–H, N–H, C–H (aromatic), C=O, C=N, C=C, C–O, C–N and C–C were identified in the ranges of 3639–3638 cm^{-1}, 3297–3137 cm^{-1}, 3188–3058 cm^{-1}, 1768–1719 cm^{-1}, 1686–1608 cm^{-1}, 1606–1495 cm^{-1}, 1503–1437 cm^{-1}, 1496–1369 cm^{-1} and 1446–1294 cm^{-1} respectively. The ^{1}H-NMR spectra of the synthesized compounds exhibited a signal with one proton integration at δ 11.319–11.721 ppm, which was attributed to the N–H protons. The ^{1}H-NMR spectra displayed signals corresponding to the aromatic protons of the quinazoline ring for compounds **7a**–**7o**, appearing as singlets, doublets, or doublets of doublets in the range of 8.875 to 2.389 ppm. Other protons were observed at their expected chemical shifts. The ^{13}C-NMR spectra of the synthesized compounds revealed two peaks at δ 160–158 ppm, which were assigned to the carbonyl and C-2 quinazoline motif, respectively. Additionally, signals for the methyl group were detected at δ 36–21 ppm. Other carbon atoms appeared at their anticipated chemical shifts. Detailed spectroscopic data is provided in the supplementary file.

Biological assessments

Antiproliferative activity potential measurement

Fifteen 3-substituted phenyl Quinazolinone derivatives (**7a**–**7o**) with different electron profile in position 3 of quinazolinone scaffold were designed and assesses as potential anti-proliferative agents towards three cancerous cell lines like, Breast (MCF-7), Colorectal (sw480) and Lung (A-549) cell lines through in vitro colorimetric MTT assay. As dedicated in Table 2, the best cytotoxic potential is coming back to **7j** with IC_{50} value of 10.0.1 ± 5.5 μM compared to Cisplatin (9.90 ± 0.27) and Erlotinib (15.25 ± 01.1) as positive drugs against MCF-7 cell line. Also, **7k** displayed a promising activity as well as Cisplatin toward all studied cell line. Preliminary screening demonstrated that approximately, most of the compounds showed higher activity in MCF-7, followed by SW480 and less in A-549. To achievement the better relationship between the structure and activity effectiveness, the compounds are divided in to two categories based on substitution at quinazoline motif. In the first category, dichloro quinazoline scaffold (**7a**–**7h**), **7c** containing hydrazine and 4-chloro phenyl at position 2 and 3 of quinazoline ring, showed moderate activity with IC_{50} = 25.85 ± 1.20 μM against A549 cell line.

Table 1 The score binding (kcal/mol) and the detailed interactions of the all designed analogues within EGFR target (1M17)

Entry	Binding energy (kcal/mol)	Amino Acid	Ligand involved moiety	Type of interaction
7a	− 8.2	Leu 820, Phe 699, Leu 694, Val 702, Asp 831, Val 702, Ala 719, Leu 694, Met 769 Thr 766, Gln 767, Leu 768, Lys 721, Gly 695	Quinazoline & phenyl moiety	Pi interactions: pi-Anion, Pi-Pi Stacked, pi-alkyl, pi-sigma Vander waals
7b	− 8.9	Leu 820, Phe 699, Leu 694, Val 702, Asp 831, Val 702, Ala 719, Met 769 Gly 697, Gly 695, Thr 766, Lys 721 Gln 767, Leu 768	Quinazoline & phenyl moiety	Pi interactions: pi-Anion, Pi-Pi Stacked, pi-alkyl Vander waals
7c	− 8.8	Leu 820, Phe 699, Leu 694, Val 702, Asp 831, Val 702, Ala 719, Met 769 Gly 695, Thr 766, Lys 721, Gln 767, Leu 768	Quinazoline & phenyl moiety	Pi interactions: pi-alkyl, pi-sigma Vander waals
7d	− 9.0	Phe 699, Val 702, Val 702, Ala 719 Gly 695, Thr 766, Thr 830, Gln 767, Leu 768, Leu 820, Leu 694, Met 769, Gly 772	Quinazoline & phenyl moiety	Pi interactions: pi-Anion, Pi-Pi Stacked, pi-alkyl Vander waals
7e	− 8.2	Leu 820, Phe 699, Leu 694, Val 702, Asp 831, Ala 719, Leu 694, Met 769, Leu 768 Thr 830, Gln 767, Pro 770, Lys 721, Gly 772, Glu 738	Quinazoline & phenyl moiety	Pi interactions: pi-Anion, Pi-Pi Stacked, pi-alkyl, pi-sigma Vander waals
7f	–	Leu 820, Phe 699, Leu 694, Val 702, Asp 831, Ala 719, Leu 694 Gly 772, Leu 768, Gln 767, Thr 766, Leu764, Glu 738, Lys 721, Thr 830	Quinazoline & phenyl moiety	Pi interactions: pi-Anion, Pi-Pi Stacked, pi-alkyl Vander waals
7g	− 9.2	Asp 831, Phe 699, Val 702, Ala 719, Lys 721, Leu 820, Leu 694 Gly 695, Gly 697, Thr 830, Gly 772, Met 769, Cys 773, Thr 766	Quinazoline & phenyl moiety	Pi interactions: pi-Anion, pi-alkyl Vander waals
7h	− 8.6	Asp 831, Met 42, Phe 699, Val 702, Ala 719, Lys 721, Lue 820 Cys 751, Gly 772, Met 769, Thr 766	Quinazoline & phenyl moiety	Pi interactions: pi Anion, Pi-Sulfur, Pi-Pi Stacedk, Pi-Alkyl Vander waals
7i	− 9.7	Asp 831 Leu 768, LEU 820, Val 702, Leu 694, Ala 719 Met 769, Thr 766, Thr 830, Glu 738, Lys 721, Phe 699	hydrazine moiety Quinazoline & phenyl moiety	Hydrogen bond Pi interactions: pi-sigma, pi- alkyl Vander waals
7j	− 9.7	Thr 830, Asp 831 Leu 820, Phe 699, Leu 694, Val 702 Gly 772, Lys 721, Met 769,	hydrazine moiety Quinazoline & phenyl moiety	Hydrogen bond Pi interactions (pi-Anion, Pi-Pi Stacked, pi-alkyl Vander waals
7k	− 10.1	Thr 830, Asp 831 Leu 820, Phe 699, Leu 694, Val 702 Gly 772, Lys 721, Met 769	hydrazine moiety Quinazoline & phenyl moiety	Hydrogen bond Pi interactions: pi-Anion, Pi-Pi Stacked, pi-alkyl Vander waals
7l	− 9.9	Arg 817 Leu 694, Val 702, Leu 820, Leu 764, Lys 721, Met 742 Gly 772, Met 769, Ala 719, Thr 766, Glu 738, Asp 831, Thr 830, Cys 773, Asn 818	Dimethyl Urea moiety Quinazoline & phenyl moiety	Hydrogen bond Pi interactions: pi-sigma, pi-alkyl Vander waals
7m	− 9.4	Lys 721 Asp 831, Val 702, Ala 719, Leu 764, Met 742 Phe 699, Thr 766, Leu 820, Gly 772, Cys 773, Arg 817	C=O moiety Quinazoline & phenyl moiety	Hydrogen bond Pi interactions: pi-sigma, pi-alkyl, pi-Anion Vander waals
7n	− 9.3	Asp 831, Val 702, Phe 699, Leu 694, Leu 820, Lys 721 Thr 830, Ala 719, Pro 770, Met 769, Leu 768, Gly 772	Quinazoline & phenyl moiety	Pi interactions: pi-sigma, pi-alkyl, pi-Anion Vander waals
7o	− 9.6	Leu 694, Leu 820, Leu 764, Met 742, Lys 721, Asp 831, Val 702 Gly 695, Phe 699, Met 769, Gly 772, Ala 719, Thr 766, Glu 738, Thr 830, Cys 773	Quinazoline & phenyl moiety	Pi interactions: pi-alkyl, pi-Anion Vander waals

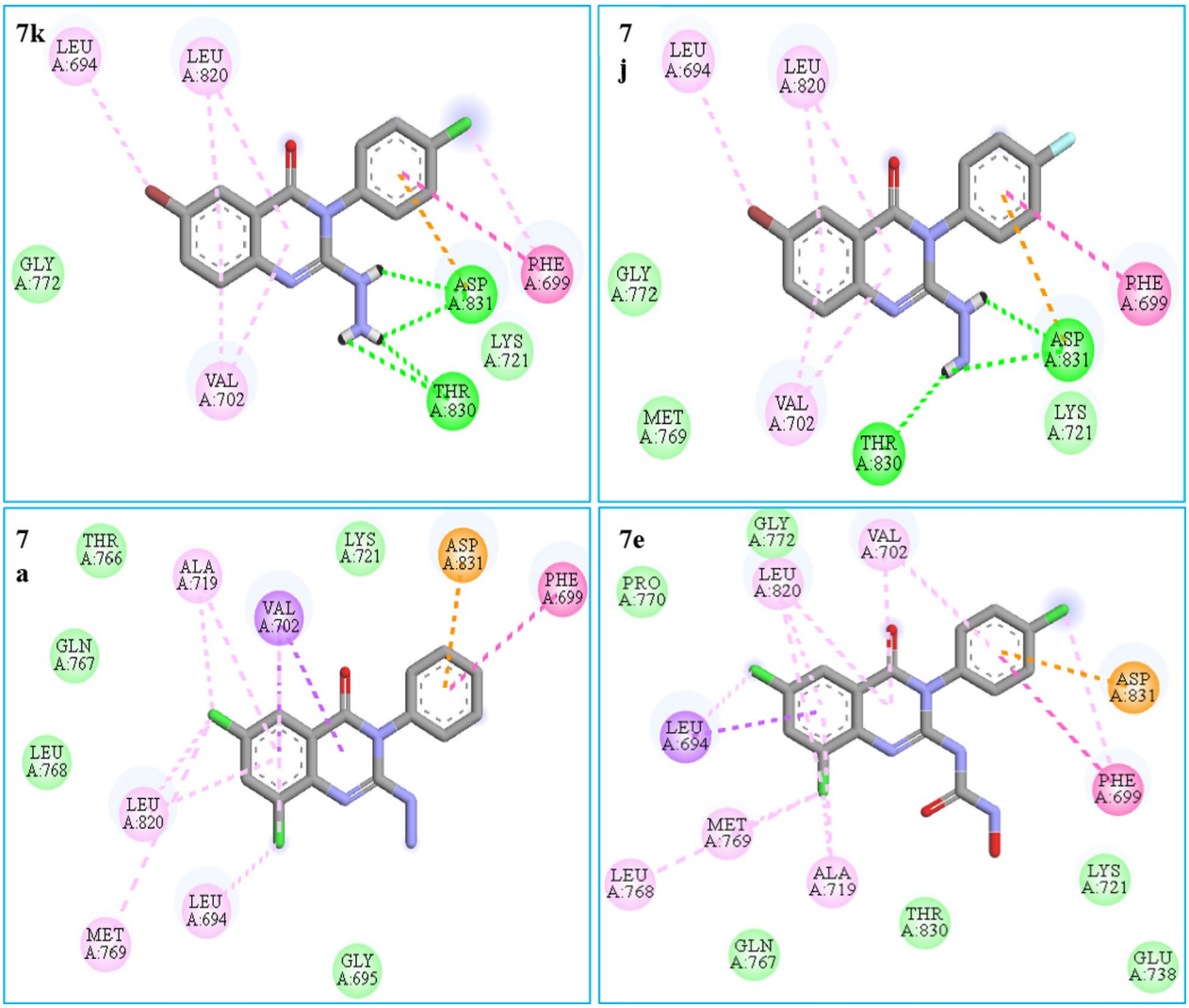

Fig. 4. 2D interaction pattern of **7k, 7j, 7a** and **7e** in the EGFR active site. Dark green and dark-pink, light pink, orange, purple and green colored amino acids represent their contribution to hydrogen bonds, pi-pi, CH-pi, pi-anion, pi-sigma and hydrophobic interactions

Incorporation of halogen substitutions on 2-hydrazine quinazoline ring (**7a**–**7c**) led to increment in cytotoxic potential. In contrast, the presence electronegative group on 2-hydroxyurea quinazoline ring (**7d**–**7e**) caused to diminish the activity. On other hand, the high value of IC_{50} in compounds (**7g** and **7h**) represents that bulky substitution at hydrazine moiety inducted to decrease the effectiveness in all studied cell lines.

Considering second category (6-Bromo-quinazoline) (**7i**–**7o**), **7j** and **7k** demonstrated considerable activity by 6 folds improvement compared to Erlotinib against MCF-7 cell line. These higher potencies, are may be as result of better hydrogen bonding and well accommodation within the EGFR active site. In 2-hydrazine quinazoline derivatives (**7i**–**7k**), the electronegative groups on phenyl moiety tend to enhance the activity in order of F > Cl compared to unsubstituted derivative (**7i**). As same as the first category, it is worth noting that the presence of any substitution on the hydrazine moiety led to significantly decrease the activity. The other point is that replacement of di-chlorine with bromine on quinazoline ring confirming the beneficial role of existence of mono-electronegative substitution on quinazoline pharmacophore for cytotoxic activity. The value of IC_{50} on NIH/3T3 fibroblast cell line showed the desirable selectivity between tumorigenic and non-tumorigenic cell line. Structure activity relationship suggested that the absence of substitution on hydrazine moiety reduces steric hindrance and led to improve the activity. Also, it was observed that the presence of di

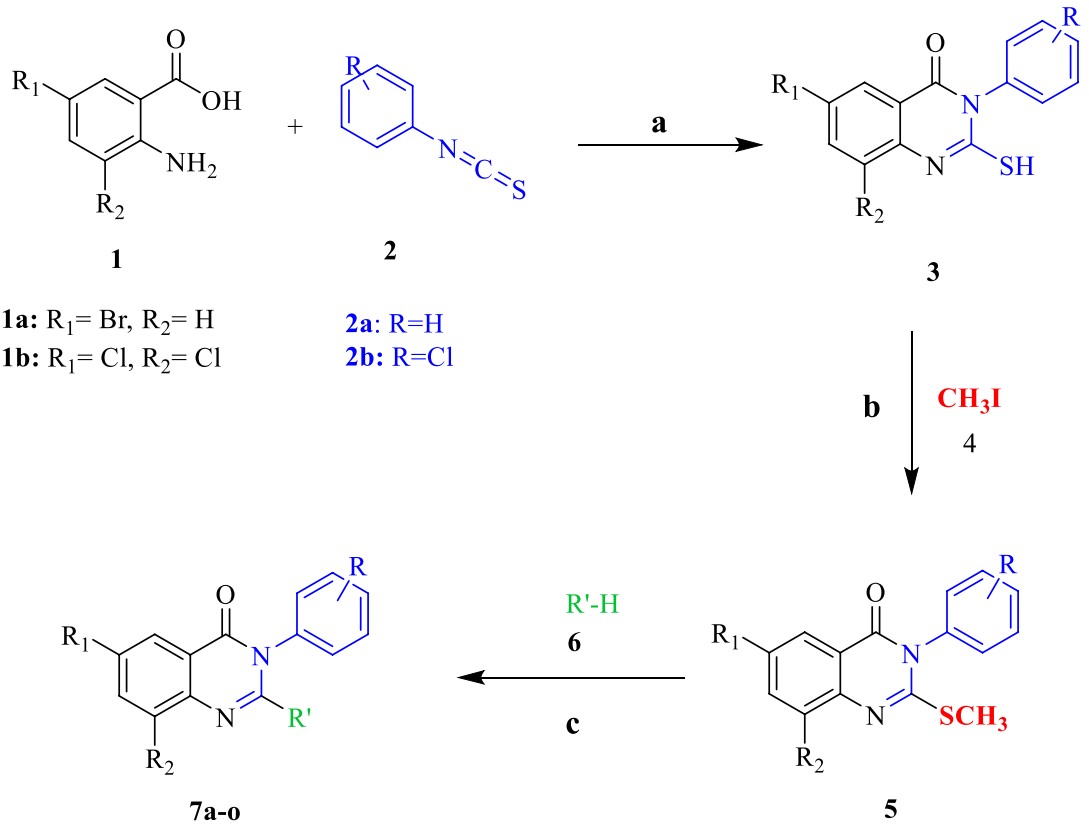

7a: R_1 = Cl, R_2 = Cl, R = H, R' = NH-NH_2
7b: R_1 = Cl, R_2 = Cl, R = 4-F, R' = NH-NH_2
7c: R_1 = Cl, R_2 = Cl, R = 4-Cl, R' = NH-NH_2
7d: R_1 = Cl, R_2 = Cl, R = H, R' = NHCONH(OH)
7e: R_1 = Cl, R_2 = Cl, R = 4-Cl, R '= NHCONH(OH)
7f: R_1 = Cl, R_2 = Cl, R=4-Cl, R' = NHCONH$(CH_3)_2$
7g: R_1 = Cl, R_2 = Cl, R = H, R' = NH-NH(C_6H_4)p-CH_3
7h: R_1 = Cl, R_2 = Cl, R = H, R' = NH-NH(C_6H_4)m-Cl
7i: R_1 = Br, R_2 = H, R = H, R' = NH-NH_2
7j: R_1 = Br, R_2 = H, R = 4-F, R' = NH-NH_2
7k: R_1 = Br, R_2 = H, R = 4-Cl, R' = NH-NH_2
7l: R_1 = Br, R_2 = H, R = H, R' = NHCONH(OH)
7m: R_1 = Br,R_2 = H, R = H, R' = NHCONH$(CH_3)_2$
7n: R_1 = Br, R_2 = H, R = H, R '= NH-NH(C_6H_4)p-CH_3
7o: R_1 = Br, R_2 = H, R = 4-Cl, R' = NH-NH(C_6H_4)m-Cl

Fig. 5 Synthesis of compounds **7a**–**7o**. Reagents and conditions: **a** EtOH, TEA, 70 ℃, 24 h; **b** DMF, K_2CO_3, 100 ℃, 24 h. **c** DMF, K_2CO_3, 100 ℃, 20 h

chlorine substitution on quinazoline ring considerably dropped in activity in comparison to mono-substituted bromine at quinazoline moiety. On the other hand, the presence of electronegative group in order to F > Cl is more favorable for phenyl moiety due to electronic profile. Finally, incorporation of substituted urea showed lower cytotoxic effects compared to hydrazine group (Fig. 6).

Apoptotic outputs

Flow cytometry Annexin V-Propodium Iodide (PI) double staining technique was applied to determine the apoptosis effect of **7k**. As could be seen at Fig. 7, the apoptosis diagram was divided to four staining part, (Av^{neg}/PI^{neg}):viable:, (Av^{pos}/PI^{neg} early apoptotic, (Av^{pos}/PI^{pos}): late apoptotic and (Av^{neg}/PI^{pos}): necrotic cells. The phosphatidylserine migration to the outer membrane was detected by fluorochrome-labeled AV. PI used as DNA dye, which detect dead and live cells in apoptosis process. The MCF-7 cell line was treated with three different concentrations of **7k** (5 µM, 10 µM, and 20 µM) for 72 h. The findings showed that **7k** induce apoptosis in MCF-7 cell line and the percentages of cells was increased from 4.5% (untreated cell) to 17.46% (5 µM), 41.2% (10 µM), and 56% (20 µM) treatment. This result demonstrated that the apoptotic effect of **7k** in the MCF-7 cell line is in dose dependent manner.

Table 2 Anticancer activity ($IC_{50} \pm SD$ (μM)) of all the synthesized compounds

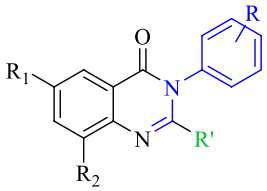

Entry	R_1	R_2	R	R′	$IC_{50} \pm SD$ (μM)[a]			
					MCF-7	SW480	A-549	NIH/3T3
7a	Cl	Cl	H	hydrazine	> 200	> 200	> 200	ND
7b	Cl	Cl	4-F	hydrazine	> 200	52.05 ± 4.17	80.05 ± 9.89	73.70 ± 2.40
7c	Cl	Cl	4-Cl	hydrazine	> 200	> 200	25.85 ± 1.20	48.55 ± 8.41
7d	Cl	Cl	H	hydroxyurea	> 200	> 200	45.10 ± 1.97	ND
7e	Cl	Cl	4-Cl	hydroxyurea	> 200	> 200	> 200	ND
7f	Cl	Cl	H	dimethylurea	> 200	> 200	> 200	38.25 ± 3.18
7g	Cl	Cl	H	p-tolylhydrazine	> 200	131.90 ± 5.09	> 200	ND
7h	Cl	Cl	H	(3-chlorophenyl) hydrazine	> 200	> 200	> 200	ND
7i	Br	H	H	hydrazine	46.35 ± 4.03	136.25 ± 1.76	53.5 ± 0.70	102.5 ± 7.07
7j	Br	H	4-F	hydrazine	10.01 ± 5.5	14.65 ± 5.44	63.85 ± 6.57	> 200
7k	Br	H	4-Cl	hydrazine	12.84 ± 0.84	10.90 ± 0.84	79.25 ± 5.30	19.70 ± 8.06
7l	Br	H	H	hydroxyurea	29.60 ± 2.26	> 200	28.00 ± 9.89	121.65 ± 11.52
7m	Br	H	H	dimethylurea	108.75 ± 5.30	> 200	31.08 ± 3.25	ND
7n	Br	H	H	p-tolylhydrazine	> 200	85.35 ± 0.63	17.40 ± 1.41	14.85 ± 1.90
7o	Br	H	4-Cl	(3-chlorophenyl) hydrazine	165.65 ± 6.85	69.50 ± 7.77	> 200	26.75 ± 0.35
Cisplatin	–	–	–	–	9.90 ± 0.27	15.25 ± 1.1	–	–
Erlotinib	–	–	–	–	39.30 ± 1.13	11.18 ± 0.38	–	–

ND: Not Determined

Cell cycle results

The cell cycle distribution of the **7k** as the most potent derivative on MCF-7 cell line was performed. The three various concentrations of **7k** (5 μM, 10 μM, and 20 μM) were treated on MCF-7 cell line for 72 h and the related cell cycle is shown in Fig. 8. After 72 h of incubation, the accumulation of the cells with 5 μM, 10 μM, and 20 μM were increased (16.66%, 25.65% and 30.61%) versus untreated cells (15.93%). This fact demonstrated that the cells could probably arrest in S phase.

Computational studies

Molecular dynamic simulation outputs

To find out the ability of biophysical structural stability of ligand–protein complex, molecular dynamic simulation was done. Also, it was applied to validate the results of molecular docking outputs. The RMSD value within 100-ns for the **7a** and **7k** modeled complex is shown in Fig. 9. Firstly, the RMSD values of the all two systems increases and approximately after 35 ns, **7k** modeled complex reached a plateau. It means that this ligand exhibited consistent stability through the active site of the EGFR protein and both of the systems reached equilibrium from 80 ns.

Flexibility and the fluctuations of amino acids involved in modeled complex was displayed via the RMSF analysis diagram. Increasing in RMSF value represents higher fluctuations and movement of the amino acids of protein within the simulation time. On the contrary, decreasing in RMSF value showed less conformational changes and also, indicated the stability of the modeled complex with the ligand. As dedicated in Fig. 10, almost, the fluctuations of most amino acids are between 0.2 and 0.5 nm during the simulation time and, **7a** and **7k** modeled complex displayed the similar patterns. The binding pocket residues were Tyr 631, Val 656, Trp 659, Tyr 662, Tyr 666 and Val 711, Tyr 547, Tyr 631, Pro 550, Phe 357, Arg 358 and Arg 125 that represented to be stable, since the RMSF values were not fluctuated much and were below 0.3 nm. The residues with high RMSF value were between 967 until 994 which that they weren't in the active site of EGFR protein. In overall, the RMSF plot showed that the ligand–protein complex had no significantly effect on the backbone of EGFR protein.

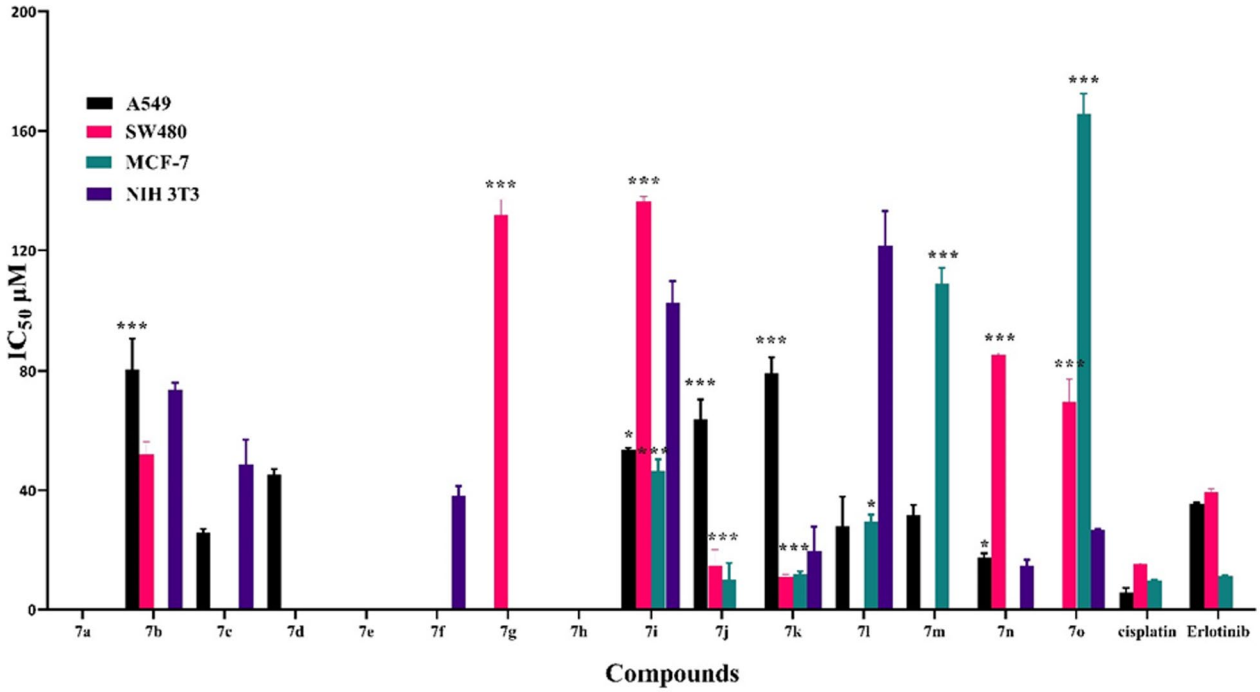

Fig. 6 Cytotoxic activity of all the synthesized compounds against MCF-7, A-549, SW480 and NIH/3T3 cell lines

The compactness of modeled complex is assessments via the gyration radius plot through the simulation time (Fig. 11). The initial values of Rg for the **7a** and **7k** were 2.28 nm and in ranging between 2.10 nm and 2.5 nm. After 25 ns of the simulation time, the Rg of the protein in two complexes were stable without any fluctuation. The lower values of Rg proved the stability and the higher compactness of the protein backbone. The Rg pattern for both selected compounds are similar that shows both of them have approximately identical in compactness, ligand affinity and stability of complex.

The number of hydrogen bonds evaluated the intermolecular hydrogen bond's ability of the ligands during the simulation period in the active site of protein. The number of hydrogen bonds for **7k**, is varying between 0 and 4 (Fig. 12) and demonstrated the strong conjugation between **7k** and EGFR protein. The average of number of hydrogen bonded interactions for **7a** and **7k** complexes were seen to be 1.026 and 1.29, respectively.

DFT results

The optimized structures of the **7k** and **7h** compounds in the gas phase are shown in Fig. 13. The molecular electric dipole moment ($\mu 0$) and polarizability (α) are shown in Table 3.

Thermodynamic properties of compounds **7k** and **7h** including total energy (E_{tot}), enthalpy (H), gibbs free energy (G), entropy (S), and heat capacity (C_v), are calculated and listed in Table 3.

Molecular orbital (MO) theory provides a powerful verification tool for stability and reactivity of the highest occupied molecular orbital (HOMO) and the lowest unoccupied molecular orbital (LUMO) (Fig. 14). MO framework allows the calculation of several global quantum molecular descriptors such as HOMO–LUMO gap (E_{gap}), global (or chemical) hardness (η), softness (σ), chemical potential (μ), and electrophilicity (ω), ionization energy (I) and electron affinity (A) (see Table 4): [44].

$$\eta = \frac{(E_{LUMO} - E_{HOMO})}{2} \tag{1}$$

$$\mu = -\frac{(E_{HOMO} + E_{LUMO})}{2} \tag{2}$$

$$\omega = \frac{\mu^2}{2\eta} \tag{3}$$

The HOMO–LUMO energy gap ($\Delta E_{tot} = E_{LUMO} - E_{HOMO}$) plays a significant role in determining several properties of molecules, including their stability and reactivity. Energy gap calculations of HOMO and LUMO orbitals show that compound **7k**, which exhibits more cytotoxic effect, has a smaller gap (as much as 0.02 eV) compared to compound **7h**.

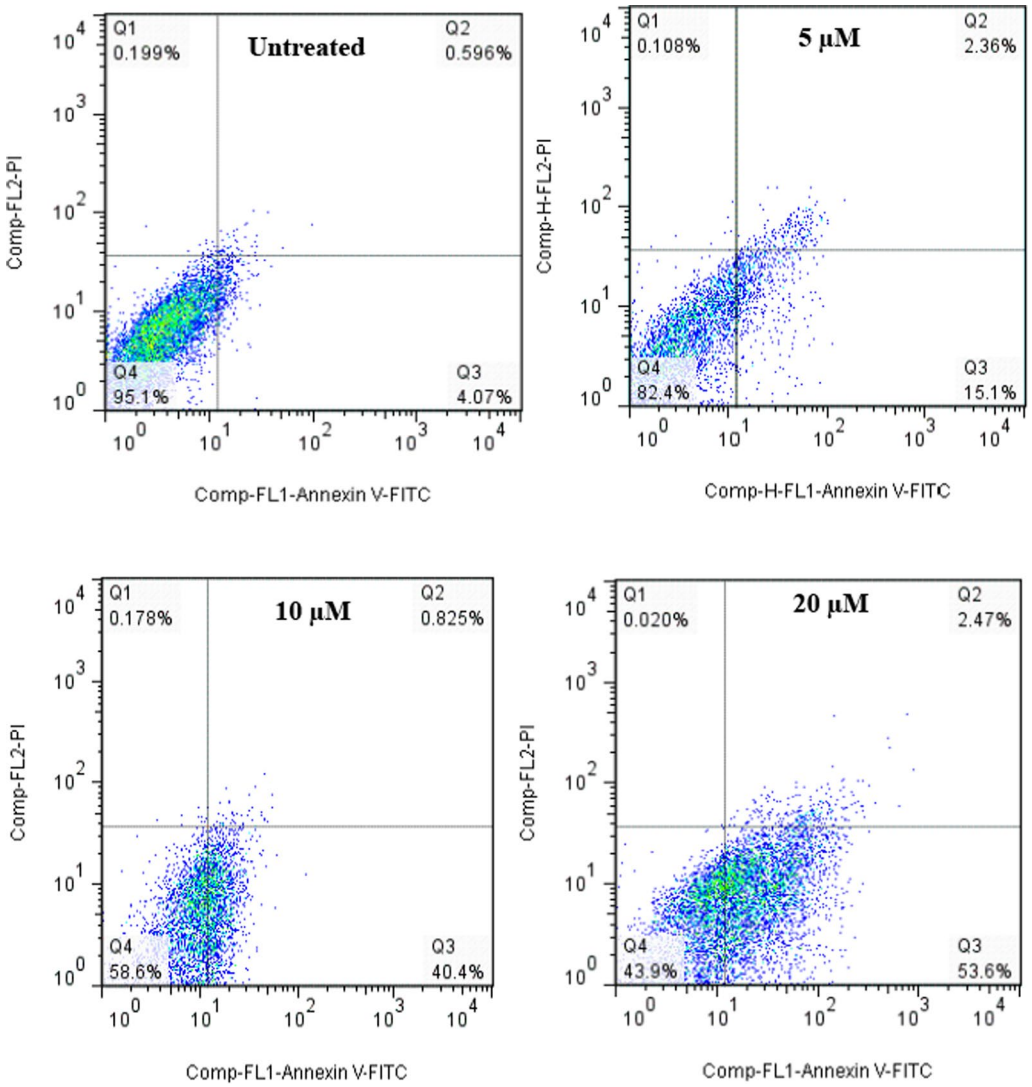

Fig. 7 Flow cytometry analysis of the apoptotic effect of **7k** on MCF-7 cell line for 72 h

A smaller energy gap between the HOMO and LUMO enhances molecular stability, facilitating easier electron transitions to excited states. Compounds with narrower energy gaps are more polarized and demonstrate increased biological activity. For instance, studies have shown that acrylic acid, with a calculated energy gap of 5.545 eV, reflects its chemical activity, suggesting that lower values correlate with higher reactivity [45].

Accordingly, compound **7k** with lower ΔE_{tot} can be a better drug in comparison to compound **7h**.

The global molecular reactivity descriptors of conceptual DFT are related to the energy gap and give deeper insight into the reactivity and stability of molecules. Table 4 shows that compound **7k** has lower chemical hardness η and higher chemical softness σ.

The molecular electrostatic potential (MEP) contour of **7k** and **7h** are shown in Fig. 15. The different values of the electrostatic potential at the surface are represented by different colors. Red parts of the surface refer to the sites for electrophilic reactions with negative ESP, blue parts represent nucleophilic sites with positive ESP and the green parts correspond to zero ESP, i.e., the neutral portions of the surface. Accordingly, the O atoms are the most negative sites while the NH groups form the most positive places.

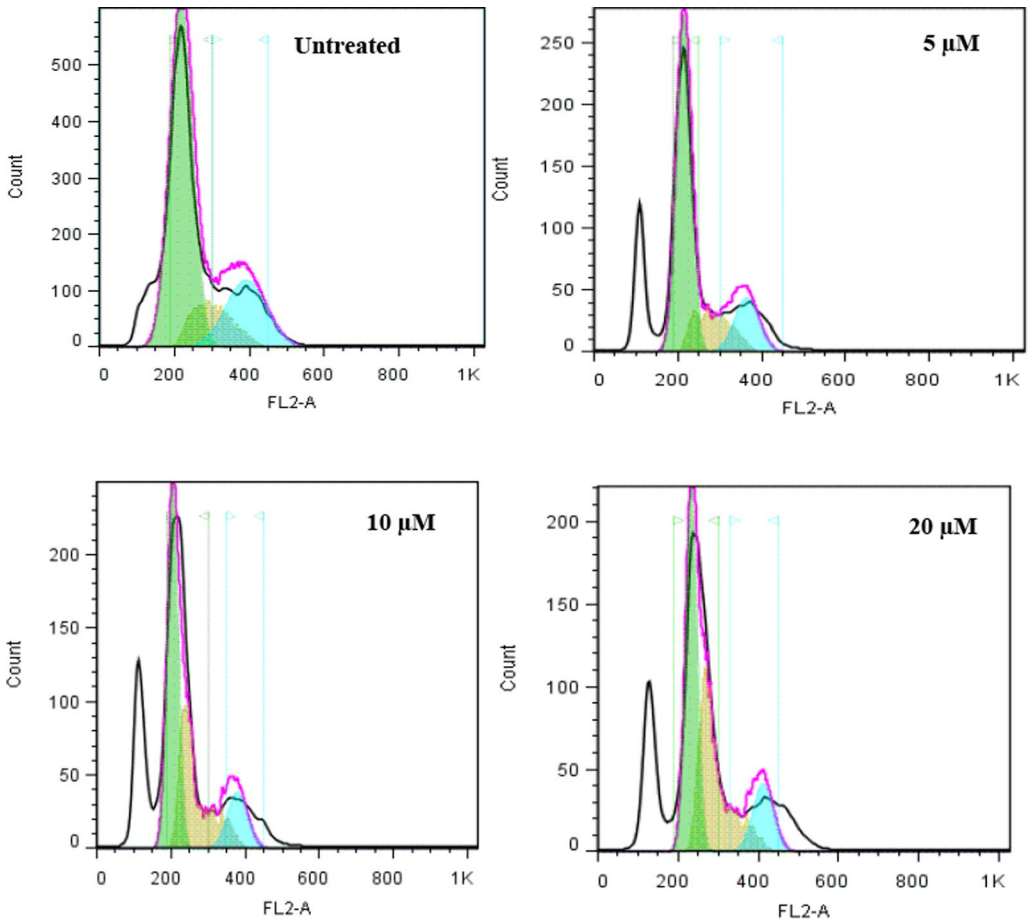

Fig. 8 The effect of **7k** on the cell cycle in the MCF-7 cell line

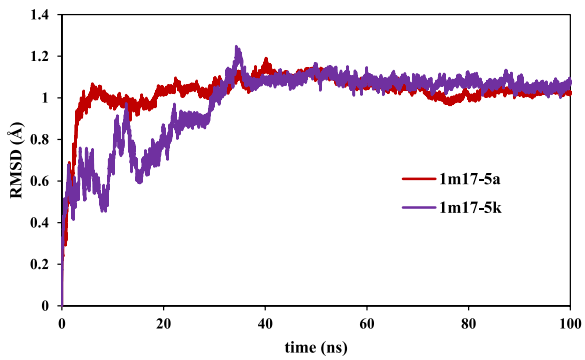

Fig. 9 RMSD plot of **7a** and **7k** of modeled complex within the simulation time

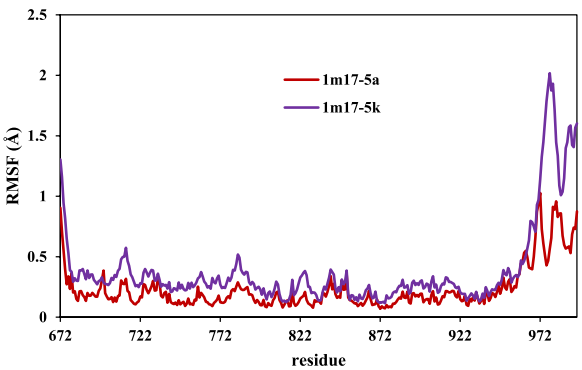

Fig. 10 The RMSF plot of the **7a** and **7k** of modeled complex during the simulation time

Physicochemical properties

Lipinski's Rule of 5 is a valuable tool in the design and discovery of new pharmaceuticals. It can be utilized to identify compounds that are likely to exhibit good oral bioavailability, thereby enhancing the likelihood of success in drug development. However, to accurately evaluate the absorption of a compound, more precise experimental and computational methods are necessary.

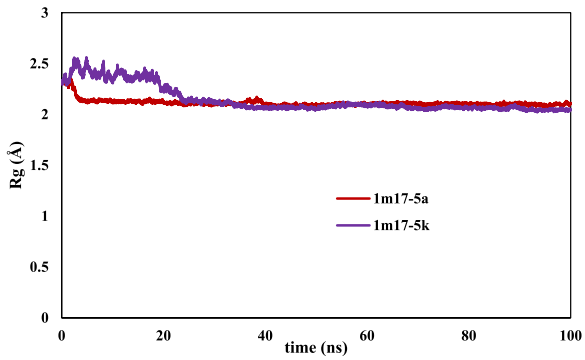

Fig. 11 The Radius of gyration (Rg) during the simulation time

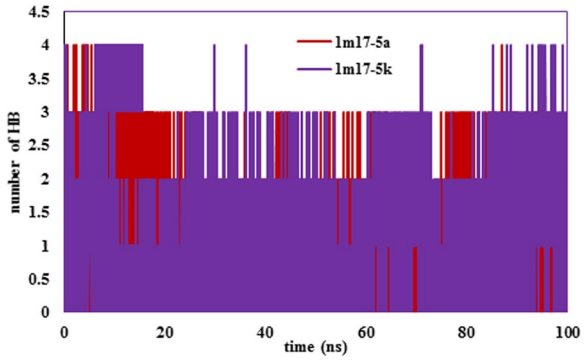

Fig. 12 The number of hydrogen bonds between the **7a** and **7k** in complex with 1M17 within the simulation time

In general, a compound should meet the following criteria to ensure good oral absorption: The molecular weight should be less than 500 g/mol, as compounds with higher molecular weights typically exhibit reduced permeability across cell membranes. The number of hydrogen bond acceptor atoms should be fewer than 5, as an increase in hydrogen bonds can diminish the compound's absorbability. Additionally, the number of hydrogen bond donor atoms should be fewer than 10; donor atoms such as nitrogen and oxygen can also influence absorbability. The logarithm of the octanol–water partition coefficient (Log P) should be less than 5. The Log P serves as an indicator of a compound's polarity. Compounds that are either highly polar or highly nonpolar generally demonstrate poor oral absorption. Although Total Polar Surface Area (TPSA) is not directly included in Lipinski's four main rules, it serves as a supplementary parameter that offers valuable insights into the polarity of a molecule and, consequently, its absorbability. Research has demonstrated that compounds with a TPSA of less than 140 $Å^2$ typically exhibit improved oral absorption. All the synthesized compounds conform to Lipinski's Rule of Five, with the exception of derivatives **7g, 7h**, and **7o**, which exhibit Log P values exceeding 5 (ranging from 5.01 to 5.39).

HIA stands for Human Intestinal Absorption. This parameter refers to the capacity of a chemical compound, such as a drug, to traverse the intestines and enter the bloodstream. The HIA is a theoretical boundary that categorizes compounds into two groups: those that are adequately absorbed and those that are poorly absorbed. The

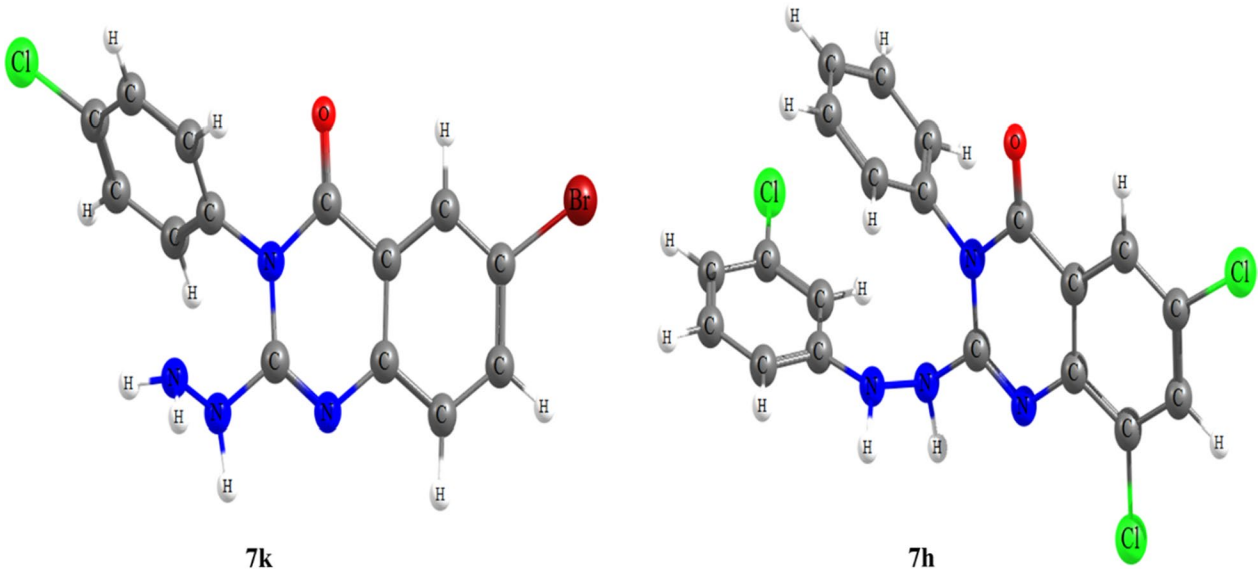

Fig. 13 The optimized structure of the **7k** and **7h** compounds in the gas phase

Table 3 Dipole moments, polarizability and thermodynamic properties of 7**k** and **7h**

Entry	$\mu 0$ (Debye)	Polarizability (α) (hartree)	Thermodynamic properties					
			E_{tot} (hartree)	*H* (hartree)	*G* (hartree)	ZPE (hartree)	*S* (Cal/mol K)	C_V (Cal/mol K)
7k	5.60	235.17	− 3865.17	− 3865.15	− 3865.22	0.22	137.54	66.29
7h	3.95	301.80	− 2444.00	− 2443.97	− 2444.05	0.29	164.95	88.56

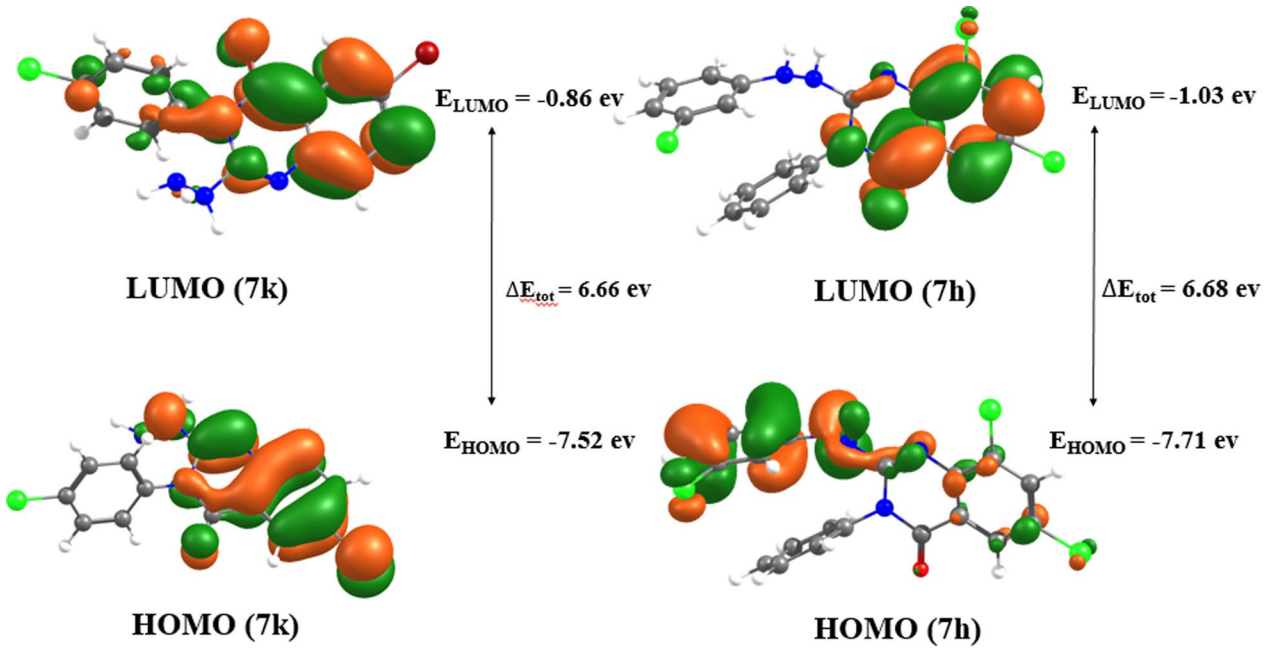

Fig. 14 Topology and energy diagram of HOMO and LUMO orbitals of **7k** and **7h** calculated at M06-2X/6–31 + G(d) level of theory

Table 4 The reactivity descriptors of compounds **7h** and **7k**

	η (ev)	σ (ev^{-1})	μ (ev)	ω (ev)	I (ev)	A (ev)
7k	3.33	0.30	4.19	2.63	7.52	0.86
7h	3.34	0.29	4.37	2.8	7.71	1.03

%HIA for the synthesized compounds ranged from 88.83 to 96.63% indicating good intestinal absorption.

The Caco-2 cell permeability test is a widely utilized laboratory method for predicting the intestinal absorption of new compounds, particularly pharmaceuticals. In this test, Caco-2 cells, which closely resemble human intestinal epithelial cells, are cultured as a monolayer on a semipermeable membrane to evaluate the new compounds. This method allows researchers to estimate the intestinal absorption of a compound before conducting clinical trials. Using this model, various factors such as molecular size, polarity, and electrical charge of the molecule can be investigated in relation to intestinal absorption. However, this method is desirable in both time-consuming and cost. Consequently, computational methods are frequently employed to predict intestinal absorption. It is important to note that these tools should complement experimental tests. The integration of these two approaches enhances the accuracy and reliability of predictions, ultimately aiding in the design of more effective drugs. All the synthesized compounds exhibited moderate intestinal absorption, ranging from 10.23 to 27.99 nm/s, indicating a reasonable level of absorption. However, derivative **5c** demonstrated a value of less than 10 nm/s, signifying poor intestinal absorption for this compound. In vitro skin permeability refers to the

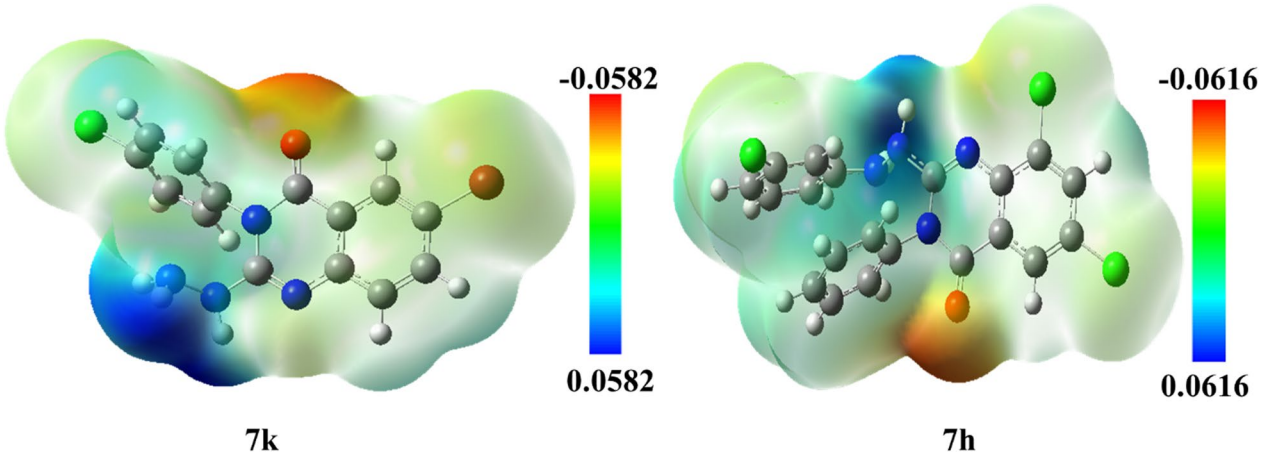

Fig. 15 MEP plots of optimized at M06–2X/6–31 + *G*(d) level of theory. blue, electrophilic sites with ⊕ ESP; red, nucleophilic sites with ⊖ ESP; green, zero ESP sites

capacity of a substance to traverse various layers of the skin and enter the body. This parameter is crucial in the development of topical medications, cosmetic products, and in the risk assessment of chemicals. The Log Kp values were assessed as negative for all compounds, indicating that these compounds did not penetrate the skin and, consequently, did not induce skin toxicity.

Plasma protein binding refers to the attachment of drugs to proteins in the blood, such as albumin. This binding significantly influences the pharmacokinetics of the drug within the body. A drug that is bound to proteins is less likely to reach its target tissues and is also excreted more slowly. The extent of protein binding affects the effective dosage of the drug, potential drug interactions, and the drug's half-life in the body. The %PPB levels for the designed compounds ranged from 84.72 to 100%.

The Blood–Brain Barrier (BBB) is a protective barrier that exists between the blood and the brain, preventing many foreign substances from entering the brain. This barrier is crucial for safeguarding the brain from toxins and infections; however, it also hinders the delivery of certain drugs to the brain. The %BBB values for most compounds fell within an acceptable range. In contrast, compounds **7g**, **7h**, **7m**, and **7o** exhibited %BBB ranging from 5.83 to 7.86%, indicating their significant penetration into the central nervous system (CNS).

As indicated by the results presented in Tables 5 and 6, compound **7k** emerged as the most effective compound, demonstrating favorable intestinal absorption with Log P value of 3.86, a TPSA of 72.94, and an %HIA of 95.67. Additionally, the percentage of PPB for this compound was less than 90%, suggesting lower binding to plasma proteins and consequently higher bioactivity.

Material and methods

Chemistry

All reagents and solvents (Merck, Sigma-Aldrich) were used as received without additional purification. Reaction progress was monitored by thin-layer chromatography (TLC) on silica gel plates pre-coated with Merck silica gel. Melting points were measured using a 9200 Electrothermal apparatus and are reported uncorrected. Nuclear magnetic resonance (NMR) spectra were recorded in DMSO-d_6 on Bruker spectrometers operating at 400 MHz for ^{1}H-NMR and 100 MHz for ^{13}C-NMR. Chemical shifts (δ) are expressed in parts per million (ppm) relative to tetramethylsilane (TMS) as the internal standard, and coupling constants (*J*) are reported in hertz (Hz). Signal multiplicities are designated as singlet (s), doublet (d), doublet of doublets (dd), triplet (t), and multiplet (m). Infrared (IR) spectra were recorded on a PerkinElmer spectrometer using the potassium bromide (KBr) pellet method.

General method for the synthesis of derivatives 2-mercapto-3-phenylquinazolin-4(3H)-one (3)

A mixture of anthranilic acid derivatives (1) (6 mmol), phenyl isothiocyanate (2) (9 mmol), and triethylamine (1.2 mL) in absolute ethanol (25 mL) was heated under reflux at 70 °C for 24 h. The progress of the reaction was monitored using thin-layer chromatography (TLC). Upon completion, the reaction mixture was filtered, and the resulting residue was recrystallized from ethanol, yielding the key intermediate 2-mercapto-3-phenylquinazolin-4(3H)-one (3) with an 83.2% yield.

Table 5 Physicochemical properties of the studied ligands

Compounds	MW (g/mol)	LogP	HBD	HBA	TPSA (Å^2)	n-RB	Lipinski violation
7a	321.16	3.47	2	3	72.94	2	0
7b	339.15	3.86	2	4	72.94	2	0
7c	355.61	3.98	2	3	72.94	2	0
7d	365.17	3.25	3	4	96.25	4	0
7e	399.62	3.75	3	4	96.25	4	0
7f	377.22	3.70	1	3	67.23	4	0
7g	411.28	5.12	2	2	58.95	4	0
7h	431.70	5.39	2	2	58.95	4	1
7i	331.17	3.35	2	3	72.94	2	0
7j	349.16	3.74	2	4	72.94	2	0
7k	365.61	3.86	2	3	72.94	2	0
7l	375.18	3.13	3	4	96.25	4	0
7m	387.23	3.59	1	3	67.23	4	0
7n	421.29	4.75	2	2	58.95	4	1
7o	441.71	5.01	2	2	58.95	4	1
Rule of Lipinski	≤ 500	≤ 5	≤ 5	≤ 10	≤ 140	≤ 10	≤ 1

Table 6 In silico ADME of studied structures

Entry	Absorption		Distribution		
Compounds	**%HIA**	**In vitro Caco-2 cell permeability (nm s^{-1})**	**In vitro skin permeability (LogKp, cm s^{-1})**	**% In vitro plasma protein binding**	**%BBB**
7a	95.27	11.93	− 3.37	91.12	1.04
7b	95.28	12.84	− 3.65	86.49	1.03
7c	95.83	6.51	− 3.25	90.69	1.68
7d	92.87	15.49	− 4.25	97.91	1.15
7e	93.98	10.23	− 4.10	95.12	1.99
7f	96.63	25.13	− 3.28	100	0.136
7g	95.79	27.15	− 2.46	95.95	7.45
7h	95.88	27.99	− 2.43	94.96	7.86
7i	95.08	17.99	− 3.36	87.52	0.76
7j	95.10	19.09	− 3.63	84.72	0.73
7k	95.67	16.72	− 3.38	89.30	1.06
7l	88.83	18.97	− 4.30	97.20	1.06
7m	96.50	25.99	− 3.23	96.67	0.08
7n	95.73	25.62	− 2.43	93.34	5.83
7o	95.85	26.22	− 2.51	96.09	6.37

General procedure for the synthesis of 2-methylthio-3-phenylquinazolin-4(3H)-one (5)

2-mercapto-3-phenylquinazolin-4(3H)-one (3) (1 mmol) was dissolved in 10 mL of dimethylformamide (DMF). Potassium carbonate (K_2CO_3, 1.2 mmol) was added gradually over a period of 5 min. Subsequently, methyl iodide (5 mmol) was introduced to the reaction mixture. The reaction was then heated under reflux for 4 h and the progress was monitored by (TLC) to give product 2-methyl-3-phenylquinazolin-4(3H)-one derivatives.

General procedure for the synthesis of compounds 7a–o

To synthesize the 3-phenylquinazolin-4(3H)-one derivatives **7a**–**7o**, 2-methyl-3-phenylquinazolin-4(3H)-one derivatives (1 mmol) from the previous step was dissolved in 10 mL of DMF. Potassium carbonate (K_2CO_3, 1.2 mmol) was gradually added over a period

of 5 min. Subsequently, hydrazine and urea derivatives (2 mmol) were introduced to the reaction mixture. The reaction was heated under reflux for 20 h, with progress monitored by TLC. Upon completion, the reaction was quenched by the addition of crushed ice, and the resulting precipitate was collected by filtration, dried, and purified. This method yielded the 3-phenylquinazolin-4(3H)-one derivatives **7a**–**7o** in yields ranging from 76.5% to 89%.

*6,8-dichloro-2-hydrazineyl-3-phenylquinazolin-4(3H)-one (**7a**)* White solid, yield: 89.4%, m.p.: 295–297 ℃, IR (KBr) ν (cm^{-1}): 3249.06 (NH), 3186.59 (C–H, aromatic), 1686.76 (C=O), 1602.31 (C=C), 1487.30 (C–O), 1433.91 (C–N), 1368.72 (C–C), 766.84 (C–Cl), 701.43 (C–Cl). ^{1}H-NMR (400 MHz, DMSO) δ (ppm): 11.327 (s, 1H, NH), 8.050 (d, *J* = 2.4 Hz, 1H, H_7-quinazoline), 7.879 (d, *J* = 2.4 Hz, 1H, H_5-quinazoline), 7.526–7.447 (m, 3H, phenyl), 7.356–7.336 (m, 2H, phenyl. ^{13}C-NMR (100 MHz, DMSO) δ (ppm): 161.116, 158.520, 150.376, 135.945, 134.737, 129.383, 129.340, 128.797, 126.627, 126.215, 120.803, 117.906.

*6,8-dichloro-3-(4-fluorophenyl)-2-hydrazineylquinazolin-4(3H)-one (**7b**)* White solid, yield: 85.6%, m.p.: 283–285 ℃, IR (KBr) ν (cm^{-1}): 3240.39 (NH), 3188.50 (C–H, aromatic), 1679.32 (C=O), 1605.12 (C=C), 1503.08 (C–O), 1433.73 (C–N), 1371.74 (C–C), 1155.07 (C–F), 759.17 (C–Cl).^{1}H-NMR (400 MHz, DMSO) δ (ppm): 11.363 (s, 1H, NH), 8.026 (d, *J* = 2.4 Hz, 1H, H_7-quinazoline), 7.867 (d, *J* = 2.4 Hz, 1H, H_5-quinazoline), 7.420–7.385 (m, 2H, phenyl), 7.357–7.313 (m, 2H, phenyl). ^{13}C-NMR (100 MHz, DMSO) δ (ppm): 161.212, 160.918, 150.449, 136.931, 134.751, 132.168, 132.133, 131.514, 131.426, 126.568, 126.206, 120.882, 117.918, 116.340.

*6,8-dichloro-3-(4-chlorophenyl)-2-hydrazineylquinazolin-4(3H)-one (**7c**)* White solid, yield: 87.4%, m.p.: 293–295 ℃, IR (KBr) ν (cm^{-1}): 3188.11 (NH), 3077.12 (C–H, aromatic), 1677.16 (C=O), 1604.71 (C=C), 1494.40 (C–O), 1443.64 (C–N), 1371.26 (C–C), 826.79 (C–Cl), 757.71 (C–Cl). ^{1}H-NMR (400 MHz, DMSO) δ (ppm): 11.371 (s, 1H, NH), 8.058 (d, *J* = 2 Hz, 1H, H_7-quinazoline), 7.882 (d, *J* = 2.4 Hz, 1H, H_5-quinazoline), 7.581 (d, *J* = 8.8 Hz, 2H, phenyl), 7.398 (d, *J* = 8.4 Hz, 2H, phenyl).^{13}C-NMR (100 MHz, DMSO) δ (ppm): 161.008, 160.864, 150.142, 136.471, 134.875, 134.793, 133.504, 131.322, 129.472, 126.860, 126.250, 120.664, 117.944.

*1-(6,8-dichloro-4-oxo-3-phenyl-3,4-dihydroquinazolin-2-yl)-3-hydroxyurea (**7d**)* White solid, yield: 76.5%, m.p.: 272–274 ℃, IR (KBr) ν (cm^{-1}): 3639.74 (OH), 3208.12 (NH), 3070.40 (C–H, aromatic), 1670.37 (C=O), 1495.93 (C=C), 1439.25 (C–O), 1370.32 (C–N), 1310.32 (C–C), 828.12 (C–Cl). ^{1}H-NMR (400 MHz, DMSO) δ (ppm): 11.719 (s, 1H, NH), 8.000 (d, *J* = 2.4 Hz, 1H, H_7-quinazoline), 7.887 (d, *J* = 2.4 Hz, 1H, H_5-quinazoline), 7.511–7.473 (m, 2H, phenyl), 7.314–7.338 (m, 2H, phenyl), 7.202 (d, *J* = 8.8Hz, 1H phenyl). ^{13}C-NMR (100 MHz, DMSO) δ (ppm): 162.785, 161.050, 150.253, 136.494, 136.866, 134.787, 129.388, 129.334, 128.833, 126.795, 126.248, 120.656, 117.922.

*1-(6,8-dichloro-3-(4-chlorophenyl)-4-oxo-3,4-dihydroquinazolin-2-yl)-3-hydroxyurea (**7e**)* White solid, yield: 79.5%, m.p.: 292–293 ℃, IR (KBr) ν (cm^{-1}): 3639.71 (OH), 3258.25 (NH), 3083.99 (C–H, aromatic), 1676.29 (C=O), 1603.50 (C=C), 1493.80 (C–O), 1443.93 (C-N), 1368.43 (C–C), 826.46 (C–Cl), 757.68 (C–Cl). ^{1}H-NMR (400 MHz, DMSO) δ (ppm): 11.368 (s, 1H, NH), 8.055 (d, *J* = 2.4 Hz, 1H, H_7-quinazoline), 7.881 (d, *J* = 2.4 Hz, 1H, H_5-quinazoline), 7.579 (d, *J* = 8.4, 2H, phenyl), 7.396 (d, *J* = 8.8, 2H, phenyl). ^{13}C-NMR (100 MHz, DMSO) δ (ppm): 162.251, 161.034, 150.171, 136.545, 134.866, 134.808, 133.496, 131.331, 129.472, 126.823, 126.247, 120.708, 117.937.

*3-(6,8-dichloro-4-oxo-3-phenyl-3,4-dihydroquinazolin-2-yl)-1,1-dimethylurea (**7f**)* White solid, yield: 84.5%, m.p.: 289–292 ℃, IR (KBr) ν (cm^{-1}): 3262.32 (NH), 3149.06 (C–H, aromatic), 1671.12 (C=O), 1495.86 (C=C), 1440.31 (C–O), 1369.92 (C–N), 1310.29 (C–C), 764.50 (C–Cl). ^{1}H-NMR (400 MHz, DMSO) δ (ppm): 11.321 (s, 1H, NH), 8.042 (d, *J* = 2.4 Hz, 1H, H_7-quinazoline), 7.876 (d, *J* = 2.4 Hz, 1H, H_5-quinazoline), 7.526–7.447 (m, 3H, phenyl), 7.357–7.333 (m, 2H, phenyl), 2.894 (s, 3H, CH_3), 2.735 (s, 3H, CH_3).^{13}C-NMR (100 MHz, DMSO) δ (ppm): 162.793, 161.064, 150.267, 136.529, 135.873, 134.793, 129.391, 129.335, 128.836, 126.780, 126.250, 120.670, 117.929, 36.262, 31.243.

*6,8-dichloro-3-phenyl-2-(2-(p-tolyl)hydrazineyl)quinazolin-4(3H)-one (**7g**)* White solid, yield: 78.5%, m.p.: 289–292 ℃, IR (KBr) ν (cm^{-1}): 3165.84 (NH), 3070.15 (C–H, aromatic), 1677.31 (C=O), 1537.58 (C=C), 1496.07 (C–O), 1446.04 (C–N), 1375.43 (C–C), 703.71 (C–Cl). ^{1}H-NMR (400 MHz, DMSO) δ (ppm): 11.319 (s, 1H, NH), 8.016 (d, *J* = 2.4 Hz, 1H, H_7-quinazoline), 7.860 (d, *J* = 2.4 Hz, 1H, H_5-quinazoline), 7.597–7.578 (m, 2H, phenyl), 7.528–7.448 (m, 5H, phenyl), 7.345 (d, *J* = 7.2 Hz, 2H, phenyl), 2.54 (s, 3H, methyl). ^{13}C-NMR (100 MHz, DMSO) δ (ppm): 161.056, 160.889, 159.837, 150.288, 143.018, 136.070, 135.894, 134.764, 134.635, 130.568, 130.055, 129.617, 129.339, 128.820, 126.736, 126.226, 125.176, 122.377, 120.699, 117.898, 16.647.

*6,8-dichloro-2-(2-(3-chlorophenyl)hydrazineyl)-3-phenylquinazolin-4(3H)-one (**7h**)* White solid, yield: 89.4%, m.p.: 279–281 ℃, IR (KBr) ν (cm^{-1}): 3286.54 (NH), 3168.74 (C–H, aromatic), 1673.71 (C=O), 1531.66 (C=C), 1437.38 (C–O), 1404.73 (C–N), 1296.04 (C–C), 784.27 (C–Cl), 705.73 (C–Cl). ^{1}H-NMR (400 MHz, DMSO) δ (ppm): 11.325 (s, 1H, NH), 8.028 (d, *J* = 2.8 Hz, 1H, H_7-quinazoline), 7.867 (d, *J* = 2.8 Hz, 1H, H_5-quinazoline), 7.597–7.578 (m, 2H, phenyl), 7.532–7.449 (m, 5H, phenyl), 7.360–7.338 (m, 2H, phenyl). ^{13}C-NMR (100 MHz, DMSO) δ (ppm): 161.035, 160.903, 150.242, 136.458, 136.078, 135.859, 134.794, 134.648, 131.397, 130.567, 130.054, 129.392, 129.339, 128.837, 126.810, 126.248, 125.190, 122.402, 120.634, 117.918.

*6-bromo-2-hydrazineyl-3-phenylquinazolin-4(3H)-one (**7i**)* White solid, yield: 87.5%, m.p.: 297–299 ℃, IR (KBr) ν (cm^{-1}): 3189.63 (NH), 3060.26 (C–H, aromatic), 1663.20 (C=O), 1605.25 (C=C), 1490.34 (C–O), 1436.43 (C–N), 1369.79 (C–C), 700.81 (C–Br). ^{1}H-NMR (400 MHz, DMSO) δ (ppm): 11.721 (s, 1H, NH), 7.997 (d, *J* = 2.4 Hz, 1H, H_5-quinazoline), 7.875 (dd, *J* = 8.8, 2.00 Hz, 1H, H_7-quinazoline), 7.513–7.432 (m, 3H, phenyl), 7.340–7.313 (m, 2H, phenyl), 7.201 (d, *J* = 8.8 Hz, 1H, H_8-quinazoline). ^{13}C-NMR (100 MHz, DMSO) δ (ppm): 161.634, 160.951, 150.426, 139.512, 138.207, 135.968, 129.888, 129.451, 129.308, 128.700, 118.155, 116.703, 114.386.

*6-bromo-3-(4-fluorophenyl)-2-hydrazineylquinazolin-4(3H)-one (**7j**)* White solid, yield: 82.7%, m.p.: 284–286 ℃C, IR (KBr) ν (cm^{-1}): 3242.84 (NH), 3186.56 (C–H, aromatic), 1673.04 (C=O), 1608.10 (C=C), 1504.14 (C–O), 1431.48 (C–N), 1370.29 (C–C), 1270.83 (C-F), 723.73 (C–Br). ^{1}H-NMR (400 MHz, DMSO) δ (ppm): 11.715 (s, 1H, NH), 7.998 (d, *J* = 2.4 Hz, 1H, H_5-quinazoline), 7.877 (dd, *J* = 8.8, 2.4 Hz, 1H, H_7-quinazoline), 7.413–7.338 (m, 2H, phenyl), 7.330–7.300 (m, 2H, phenyl), 7.209–7.181 (m, 1H, H_8-quinazoline). ^{13}C-NMR (100 MHz, DMSO) δ (ppm): 161.683, 160.874, 150.426, 139.485, 138.213, 132.140, 132.110, 131.615, 131.528, 129.887, 118.147, 116.675, 116.252, 116.026, 114.395.

*6-bromo-3-(4-chlorophenyl)-2-hydrazineylquinazolin-4(3H)-one (**7k**)* White solid, yield: 87.3%, m.p.: 273–275 ℃, IR (KBr) ν (cm^{-1}): 3189.12 (NH), 3065.30 (C–H, aromatic), 1671.49 (C=O), 1606.19 (C=C), 1487.59 (C–O), 1437.90 (C–N), 1369.81 (C–C), 825.24 (C–Cl), 761.45 (C–Br).^{1}H-NMR (400 MHz, DMSO) δ (ppm): 11.371(s, 1H, NH), 8.059 (d, *J* = 2.4 Hz, 1H, H_5-quinazoline), 7.884 (d, *J* = 2.4 H, H_7-quinazoline), 7.594–7.570 (m, 2H, phenyl), 7.411–7.387 (m, 2H, phenyl), 7.378 (d, 1H, *J* = 8.8 Hz, H_8-quinazoline). ^{13}C-NMR (100 MHz, DMSO) δ (ppm): 161.568, 150.280, 139.503, 138.264, 134.896, 133.343, 131.444, 129.880, 129.354, 118.183, 116.681, 114.424.

*1-(6-bromo-4-oxo-3-phenyl-3,4-dihydroquinazolin-2-yl)-3-hydroxyurea (**7l**)* White solid, yield: 79.9%, m.p.: 285–287 ℃, IR (KBr) ν (cm^{-1}) 3638.48 (OH), 3248.21 (NH), 3186.27 (C–H, aromatic), 1669.91 (C=O), 1603.28 (C=C), 1486.03 (C–O), 1427.39 (C–N), 1367.27 (C–C), 763.53 (C–Br).^{1}H-NMR (400 MHz, DMSO) δ (ppm): 11.715 (s, 1H, NH), 7.999 (d, *J* = 2.4 Hz, 1H, H_5-quinazoline), 7.878 (dd, *J* = 8.8, 2.4 Hz, 1H, H_7-quinazoline), 7.511–7.473 (m, 2H, phenyl), 7.451–7.433 (m, 1H, phenyl), 7.338–7.314 (m, 2H, phenyl), 7.199 (d, *J* = 8.8 Hz, 1H, H_8-quinazoline). ^{13}C-NMR (100 MHz, DMSO) δ (ppm): 162.640, 161.029, 150.426, 139.518, 138.213, 135.968, 129.893, 129.450, 129.306, 128.700, 118.156, 116.705, 114.385.

*3-(6-bromo-4-oxo-3-phenyl-3,4-dihydroquinazolin-2-yl)-1,1-dimethylurea (**7m**)* White solid, yield: 82.5%, m.p: 293–295 ℃, IR (KBr) ν (cm^{-1}): 3187.30 (NH, 3075.93 (C–H aromatic), 1676.19 (C=O), 1603.54 (C=C), 1493.50 (C–O), 1443.20 (C–N), 1369.19 (C–C), 757.12 (C–Br). ^{1}H-NMR (400 MHz, DMSO) δ (ppm): 11.320 (s, 1H, NH), 8.035 (dd, *J* = 2.4, 0.8 Hz, 1H, H_5-quinazoline), 7.955 (br, 1H, H_7-quinazoline), 7.875–7.867 (m, 1H, H_8-quinazoline), 7.507–7.488 (m, 3H, phenyl), 7.345 (d, *J* = 8.4 Hz, 2H, phenyl), 2.891 (s, 3H, CH_3), 2.734 (s, 3H, CH_3) .^{13}C-NMR (100 MHz, DMSO) δ (ppm): 161.634, 161.309, 150.426, 139.510, 138.205, 135.961, 129.893, 129.449, 129.307, 128.700, 118.150, 116.697, 114.389, 36.251, 32.913.

*6-bromo-3-phenyl-2-(2-(p-tolyl)hydrazineyl)quinazolin-4(3H)-one (**7n**)* White solid, yield: 76.0%, m.p.: 287–289 ℃, IR (KBr) ν (cm^{-1}): 3137.29 (NH), 2998.95 (C–H aromatic), 1677.31(C=O), 1534.59 (C=C), 1496.07 (C–O), 1446.04 (C–N), 1375.43 (C–C), 703.71 (C–Br). ^{1}H-NMR (400 MHz, DMSO) δ (ppm): 11.224 (s, 1H, NH), 8.138 (d, *J* = 2.4 Hz, 1H, H_5-quinazoline), 8.005 (dd, *J* = 8.4, 2.4 Hz, 1H, H_7-quinazoline), 7.650 (d, *J* = 8.4 Hz, 1H, H_8-quinazoline), 7.542–7.533 (m, 1H, phenyl), 7.417 (d, *J* = 6.8 Hz, 1H, phenyl), 7.360–7.275 (m, 7H, phenyl), 2.389 (s, 3H, methyl). ^{13}C-NMR (100 MHz, DMSO) δ (ppm): 160.116, 158.520, 146.715, 138.155, 137.069, 136.078, 133.744, 130.449, 129.995, 129.755, 129.472, 129.042, 128.954, 121.794, 118.447, 117.915, 21.152.

*6-bromo-2-(2-(3-chlorophenyl)hydrazineyl)-3-phenylquinazolin-4(3H)-one (**7o**)* White solid, yield: 89.5%, m.p.: 294–297 ℃, IR (KBr) ν (cm^{-1}): 3297.86 (NH), 3068.75 (C–H aromatic), 1686.75 (C=O), 1539.38 (C=C), 1444.73 (C–O), 1406.04 (C–N), 1294.27 (C–C),

783.98 (C–Cl), 705.73 (C–Br). ^{1}H-NMR (400 MHz, DMSO) δ (ppm): 11.225 (s, 1H, NH), 8.136 (d, J=2.0 Hz, 1H, H_5-quinazoline), 8.006 (dd, J=8.4, 2.4 Hz, 1H, H_7-quinazoline), 7.651 (d, J=8.8 Hz, 1H, H_8-quinazoline), 7.537 (s, 1H, phenyl), 7.417 (d, J=6.8 Hz, 1H, phenyl), 7.360–7.291 (m, 7H, phenyl). ^{13}C-NMR (100 MHz, DMSO) δ (ppm): 160.138, 158.474, 146.623, 140.227, 140.109, 138.134, 133.386, 133.263, 130.682, 130.521, 129.705, 129.467, 129.072, 128.837, 128.603, 127.693, 121.801,118.499.

Biological assay

Cytotoxic measurement

The cytotoxic effects of the synthesized derivatives (**7a**–**7h**) were evaluated using the MTT assay [46, 47]. The three cancer cell lines, MCF-7, SW480 and A549 were obtained from the National Cell Bank of Iran (NCBI). The cancer cell lines were cultured in RPMI 1640 media supplemented with 10% fetal bovine serum (FBS) and 1% penicillin–streptomycin (Gibco, USA). NIH/3T3 was obtained and cultured in DMEM high glucose (Bio Idea, Iran) in the presence of 2% L-glutamine (Gibco, USA) as normal cell line. Once the cells reached the appropriate confluence, they were harvested using a 0.5% trypsin/EDTA solution (Gibco, USA). A total of 1×10^4 cells per well were plated in 96-well microplates [48]. Various concentrations of all derivatives and Erlotinib were added to the microplates. After 48 h, the media was aspirated, and 100 µL of a freshly prepared MTT solution was added, followed by incubation for 4 h at 37 °C [49]. Subsequently, 150 µL of DMSO was added to dissolve the formazan crystals. The absorbance of all derivatives was measured at 490 nm using a microplate ELISA reader. Data analysis was performed using Excel 2016 and Curve Expert 1.4. [50].

Apoptotic assay

To assess apoptosis in SW480 cells, 5×10^4 cells were initially pre-cultured in 24-well plates using RPMI 1640 culture medium for 16 h. The cells were then treated with varying doses of the 2g complex (10.0, 20.0, and 40.0 µM). Following treatment, the cells were harvested with 0.25% trypsin and washed with phosphate-buffered saline (PBS). 5 µL of propidium iodide (1 mg/mL) and 1 unit of RNase A were added for staining. Cell cycle analysis and DNA content evaluation were performed using flow cytometry (BD FACSCalibur) and FlowJo 10.0 software to assess the apoptotic status of the cells [51].

Cell cycle assay

To assess the cell cycle, a total of 5×10^4 SW480 cells were initially pre-cultured in 24-well plates with RPMI 1640 culture medium for 16 h under standard culturing conditions. The cells were then treated with varying concentrations (10.0, 20.0, and 40.0 µM) of the 2g complex. After treatment, the cells were harvested using 0.25% trypsin, washed with PBS, and fixed in 70% ethanol for 2 h. Subsequently, the cells were centrifuged at 4000 rpm for 2 min and permeabilized with 0.2% Triton X-100 for 15 min at 4 °C. After a second round of centrifugation, the cells were resuspended in PBS containing propidium iodide and RNase A. Cell cycle analysis was performed using flow cytometry (BD FACSCalibur Flow Cytometer), and DNA content was analyzed using FlowJo 10.0 software.

Computational studies

Docking procedure

In house batch script (DOCK-FACE) was used to run the docking protocol [52] according to previous studies [53, 54]. At the first time, the structures of ligands were drawn and optimized by Molecular Mechanic (MM^+) following semi empirical AM1 method (Hyper Chem Professional Version 8 (Hypercube Inc., Gainesville, FL, USA). and then converted to PDBQT format using MGL tools 1.5.6 software [55]. The 3D crystal structure of EGFR (PDB ID: 1M17) was obtained from Protein Data Bank (PDB data base; http://www.rcsb.org) [56]. Firstly, all water molecules and co-crystal ligand were omitted and polar hydrogens were added and checked for missing atoms with MODELLER 9.17 [57]. A grid box of 70 × 70 × 70 points in in x, y, and z directions was built and centered on the ligand. Number of points in x, y and z was 20.14, and 0.3, and 52.2. For internal validation, co-crystal ligand for each receptor individually, was excluded and treated the same as examined ligand. All the docking procedures were done on validated procedure with a root mean square deviation (RMSD) value below of 2 Å. All interactions were visualized via Discovery studio client 16 software [52].

Molecular dynamics simulation

GROMACS software was applied to analyze the dynamic nature of ligand–protein complex during molecular dynamics simulation time (100 ns). The simulations were performed using an AMBER force field. Tipp3 water molecules were added to the simulation box.

Periodic boundary conditions (PBC) were applied to all three directions of the system. Firstly, steepest descent algorithm was used to minimize the energy. Afterwards, the system was equilibrated by NVT and NPT ensembles. All parameters for MD simulation were done base on our recent studies [58]. The analysis of Root Mean Square Deviation (RMSD), Root Mean Square Fluctuation (RMSF), the Radius of gyration (Rg), and the number of hydrogen bonds (HB) were analyzed within the MD 5.

DFT studies

The quantum chemical calculations in the framework of density functional theory (DFT) were used to predict the equilibrium geometry of **7k** and **7h** compounds. The geometry optimizations were performed at the M06-2X/6–31 + G(d) level for all atoms [59–61]. All calculations performed using Gaussian 09 program [62]. Calculations of zero-point vibrational energy (ZPVE) and the vibrational frequency analysis were also performed.

ADMET analysis

By utilizing the SwissADME online software and the preADMET online tool, the server (http://preadmet.bmdrc.org/) physicochemical properties. Pharmacokinetic properties, including absorption, distribution, and metabolism, Excretion was successfully achieved.

Conclusion

In this study, fifteen novel quinazoline derivative prepared by introducing different hydrazine and urea derivative at position 2 of quinazoline ring. The chemical structures were characterized using FT-IR, ^{1}HNMR, and ^{13}CNMR spectroscopy. The cytotoxic potential of all compounds was examined on three human cancerous cell lines, A549, SW480 and MCF-7. The most of the derivative revealed desirable cytotoxic activity in the range of 10.01–136.25 μM with the most potent compound (**7k**) exhibiting a promising IC_{50} values (12.84 and 10.90) compared to Erlotinib against MCF-7 and SW480 cell lines. The SAR studies suggested that presence of mono-substituted bromine and hydrazine ring at position 6 and 2 of quinazoline fragment led to increase the cytotoxic potential. On the other hand, the incorporation of electronegative substitution at phenyl moiety causes to increment in activity. Also, **7k** could induce apoptosis and cell cycle at dose dependent manner and arrest at S phase. Molecular docking findings showed that **7k** could tighter binding to active site of EGFR enzyme and the MD simulation supported these results. Compound **7k** exhibited a narrow energy gap between HOMO and LUMO along with favorable electrostatic surface potential parameters. Overall, these novel quinazoline derivatives may be considered promising candidates for use as cytotoxic inhibitors.

Supplementary Information

The online version contains supplementary material available at https://doi.org/10.1186/s13065-025-01492-4.

Supplementary Material 1.

Acknowledgements
Not applicable.

Author contributions
M.M. prepare the manuscript, and performed the computational section. L. E. contributed to perform biological section. Z. R. performed and written the simulation section. S. Kh edit the manuscript and supervise the study. All authors read and approved the final manuscript.

Funding
This investigation was financially supported by Shiraz University of Medical Sciences (Grant No.: 27124).

Availability of data and materials
The data sets used and analyzed during the current study are available from the corresponding author upon reasonable request. We have presented all data in the form of Figures. The PDB code (1M17) was retrieved from protein data bank (www.rcsb.org). https://www.rcsb.org/structure/1M17.

Declarations

Ethics approval and consent to participate
Not Applicable.

Consent for publication
Not applicable.

Competing interests
The authors declare no competing interests.

Received: 23 February 2025 Accepted: 28 April 2025
Published online: 13 May 2025

References

1. Allam HA, Aly EE, Farouk AK, El Kerdawy AM, Rashwan E, Abbass SE. Design and Synthesis of some new 2, 4, 6-trisubstituted quinazoline EGFR inhibitors as targeted anticancer agents. Bioorg Chem. 2020;98: 103726.
2. Eissa AA, Aljamal KF, Ibrahim HS, Allam HA. Design and synthesis of novel pyridopyrimidine derivatives with anchoring non-coplanar aromatic extensions of EGFR inhibitory activity. Bioorg Chem. 2021;116: 105318.
3. Celik I, Ayhan-Kılcıgil G, Guven B, Kara Z, Gurkan-Alp AS, Karayel A, et al. Design, synthesis and docking studies of benzimidazole derivatives as potential EGFR inhibitors. Eur J Med Chem. 2019;173:240–9.
4. Cheng Y, Wang L, Zhang S, Jian W, Zeng B, Liang L, et al. The investigation of Nfκb inhibitors to block cell proliferation in OSCC cells lines. Curr Med Chem. 2024. https://doi.org/10.2174/0109298673309489240816063313.
5. Debela DT, Muzazu SG, Heraro KD, Ndalama MT, Mesele BW, Haile DC, et al. New approaches and procedures for cancer treatment: current perspectives. SAGE Open Med. 2021;9:20503121211034370.
6. Liu B, Zhou H, Tan L, Siu KTH, Guan X-Y. Exploring treatment options in cancer: tumor treatment strategies. Signal Transduct Target Ther. 2024;9(1):175.

7. Lee YT, Tan YJ, Oon CE. Molecular targeted therapy: Treating cancer with specificity. Eur J Pharmacol. 2018;834:188–96.
8. Widakowich C, de Azambuja E, Gil T, Cardoso F, Dinh P, Awada A, et al. Molecular targeted therapies in breast cancer: where are we now? Int J Biochem Cell Biol. 2007;39(7–8):1375–87.
9. Li R, Luo P, Guo Y, He Y, Wang C. Clinical features, treatment, and prognosis of SGLT2 inhibitors induced acute pancreatitis. Expert Opin Drug Saf. 2024. https://doi.org/10.1080/14740338.2024.2396387.
10. Jing R, Jiang Z, Tang X. Advances in millimeter-wave treatment and its biological effects development. Int J Mol Sci. 2024;25(16):8638.
11. Ishikawa T, Seto M, Banno H, Kawakita Y, Oorui M, Taniguchi T, et al. Design and synthesis of novel human epidermal growth factor receptor 2 (HER2)/epidermal growth factor receptor (EGFR) dual inhibitors bearing a pyrrolo [3, 2-d] pyrimidine scaffold. J Med Chem. 2011;54(23):8030–50.
12. Sonousi A, Hassan RA, Osman EO, Abdou AM, Emam SH. Design and synthesis of novel quinazolinone-based derivatives as EGFR inhibitors with antitumor activity. J Enzyme Inhib Med Chem. 2022;37(1):2644–59.
13. Wang Y, Guo S, Sun W, Tu H, Tang Y, Xu Y, et al. Synthesis of 4 H-Pyrazolo [3, 4-d] pyrimidin-4-one hydrazine derivatives as a potential inhibitor for the self-assembly of TMV particles. J Agric Food Chem. 2024;72(6):2879–87.
14. Chen S, Long S, Liu Y, Wang S, Hu Q, Fu L, et al. Evaluation of a three-gene methylation model for correlating lymph node metastasis in postoperative early gastric cancer adjacent samples. Front Oncol. 2024;14:1432869.
15. Wang L, Li X, Men X, Liu X, Luo J. Research progress on antioxidants and protein aggregation inhibitors in cataract prevention and therapy. Mol Med Rep. 2024;31(1):22.
16. Abdelrahman AH, Azab ME, Hegazy MA, Labena A, Alzahrani AY, Ramadan SK. Synthesis, computational analysis, and exploring antiproliferative activity of triazolo-and thiazolo-pyrimidine derivatives as potential EGFR inhibitors. J Mol Struct. 2025;1333: 141789.
17. Zhou P, Chen G, Gao M, Wu J. Design, synthesis and evaluation of the osimertinib analogue (C-005) as potent EGFR inhibitor against NSCLC. Bioorg Med Chem. 2018;26(23–24):6135–45.
18. Normanno N, De Luca A, Bianco C, Strizzi L, Mancino M, Maiello MR, et al. Epidermal growth factor receptor (EGFR) signaling in cancer. Gene. 2006;366(1):2–16.
19. Li H-Q, Li D-D, Lu X, Xu Y-Y, Zhu H-L. Design and synthesis of 4, 6-substituted-(diaphenylamino) quinazolines as potent EGFR inhibitors with antitumor activity. Bioorg Med Chem. 2012;20(1):317–23.
20. Wu J, Chen W, Xia G, Zhang J, Shao J, Tan B, et al. Design, synthesis, and biological evaluation of novel conformationally constrained inhibitors targeting EGFR. ACS Med Chem Lett. 2013;4(10):974–8.
21. Zhao L, Weng Y, Zhou X, Wu G. Aminoselenation and dehydroaromatization of cyclohexanones with anilines and diselenides. Org Lett. 2024;26(22):4835–9.
22. Sun D-Y, Hu Y-J, Li X, Peng J, Dai Z-J, Wang S. Unlocking the full potential of memory T cells in adoptive T cell therapy for hematologic malignancies. Int Immunopharmacol. 2025;144: 113392.
23. Elgubbi AS, El-Helw EA, Alzahrani AY, Ramadan SK. Synthesis, computational chemical study, antiproliferative activity screening, and molecular docking of some thiophene-based oxadiazole, triazole, and thiazolidinone derivatives. RSC Adv. 2024;14(9):5926–40.
24. Abdelrahman AM, Fahmi AA, Rizk SA, El-Helw EA. Synthesis, DFT and antitumor activity screening of some new heterocycles derived from 2, 2'-(2-(1, 3-Diphenyl-1 H-Pyrazol-4-yl) Ethene-1, 1-Diyl) Bis (4 H-Benzo [d] [1, 3] Oxazin-4-One). Polycyclic Aromat Compd. 2023;43(1):721–39.
25. Hassaballah AI, Ramadan SK, Rizk SA, El-Helw EA, Abdelwahab SS. Ultrasonic promoted regioselective reactions of the novel spiro 3, 1-benzoxazon-isobenzofuranone dye toward some organic base reagents. Polycyclic Aromat Compd. 2023;43(4):2973–89.
26. Patel HM, Pawara R, Ansari A, Noolvi M, Surana S. Design and synthesis of quinazolinones as EGFR inhibitors to overcome EGFR resistance obstacle. Bioorg Med Chem. 2017;25(10):2713–23.
27. Guda R, Korra R, Balaji S, Palabindela R, Eerla R, Lingabathula H, et al. Design, synthesis and biological evaluation of 8-substituted-6-hydrazonoindolo [2, 1-b] quinazolin-12 (6H)-one scaffolds as potential cytotoxic agents: IDO-1 targeting molecular docking studies. Bioorg Med Chem Lett. 2017;27(20):4741–8.
28. Guda R, Narsimha S, Babu R, Muthadi S, Lingabathula H, Palabindela R, et al. Novel substituted hydrazono indolo [2, 1-b] quinazoline-6, 12-dione analogues as cytostatic agents: Synthesis, crystal structure, biological evaluation and molecular docking studies. Bioorg Med Chem Lett. 2016;26(22):5517–23.
29. Ramadan SK, Abd-Rabboh HS, Abou-Elmagd WS. Antiproliferative activity and molecular docking of some pyrazole-based quinazolinone, benzimidazole, and tetrazinethione derivatives. J Biochem Mol Toxicol. 2025;39(1): e70131.
30. Ramadan SK, Elrazaz EZ, Abouzid KA, El-Naggar AM. Design, synthesis and in silico studies of new quinazolinone derivatives as antitumor PARP-1 inhibitors. RSC Adv. 2020;10(49):29475–92.
31. Kang L, Gao X-H, Liu H-R, Men X, Wu H-N, Cui P-W, et al. Structure–activity relationship investigation of coumarin–chalcone hybrids with diverse side-chains as acetylcholinesterase and butyrylcholinesterase inhibitors. Mol Diversity. 2018;22:893–906.
32. Feng C, Wang Y, Xu J, Zheng Y, Zhou W, Wang Y, et al. Precisely tailoring molecular structure of doxorubicin prodrugs to enable stable nanoassembly, rapid activation, and potent antitumor effect. Pharmaceutics. 2024;16(12):1582.
33. Lou Y, Cheng M, Cao Q, Li K, Qin H, Bao M, et al. Simultaneous quantification of mirabegron and vibegron in human plasma by HPLC-MS/MS and its application in the clinical determination in patients with tumors associated with overactive bladder. J Pharm Biomed Anal. 2024;240: 115937.
34. Emami L, Hassani M, Mardaneh P, Zare F, Saeedi M, Emami M, et al. 6-Bromo quinazoline derivatives as cytotoxic agents: design, synthesis, molecular docking and MD simulation. BMC Chem. 2024;18(1):125.
35. Mitchell RA, Luwor RB, Burgess AW. Epidermal growth factor receptor: structure-function informing the design of anticancer therapeutics. Exp Cell Res. 2018;371(1):1–19.
36. Zubair T, Bandyopadhyay D. Small molecule EGFR inhibitors as anticancer agents: discovery, mechanisms of action, and opportunities. Int J Mol Sci. 2023;24(3):2651.
37. Wright NMA, Goss GD. Third-generation epidermal growth factor receptor tyrosine kinase inhibitors for the treatment of non-small cell lung cancer. Transl Lung Cancer Res. 2019;8(Suppl 3):S247.
38. Cheng H, Nair SK, Murray BW. Recent progress on third generation covalent EGFR inhibitors. Bioorg Med Chem Lett. 2016;26(8):1861–8.
39. Hisham M, Hassan HA, Gomaa HA, Youssif BG, Hayallah AM, Abdel-Aziz M. Structure-based design, synthesis and antiproliferative action of new quinazoline-4-one/chalcone hybrids as EGFR inhibitors. J Mol Struct. 2022;1254: 132422.
40. Mohamed AM, Abou-Ghadir OM, Mostafa YA, Almarhoon ZM, Bräse S, Youssif BG. Design, synthesis, and antiproliferative activity of new 1, 2, 3-triazole/quinazoline-4-one hybrids as dual EGFR/BRAF V600E inhibitors. RSC Adv. 2024;14(52):38403–15.
41. Hisham M, Hassan HA, Gomaa HA, Youssif BG, Hayalah AM, Abdel-Aziz M. Design, synthesis, and antiproliferative activity of quinazolin-4-one/chalcone hybrids via the EGFR inhibition pathway. Anti-Cancer Agents Med Chem. 2023;23(17):1932–43.
42. Al-Wahaibi LH, Hisham M, Abou-Zied HA, Hassan HA, Youssif BG, Bräse S, et al. Quinazolin-4-one/3-cyanopyridin-2-one hybrids as dual inhibitors of EGFR and BRAFV600E: design, synthesis, and antiproliferative activity. Pharmaceuticals. 2023;16(11):1522.
43. Bhatia P, Sharma V, Alam O, Manaithiya A, Alam P, Alam MT, et al. Novel quinazoline-based EGFR kinase inhibitors: A review focussing on SAR and molecular docking studies (2015–2019). Eur J Med Chem. 2020;204: 112640.
44. Armaković S, Armaković SJ, Vraneš M, Tot A, Gadžurić S. Determination of reactive properties of 1-butyl-3-methylimidazolium taurate ionic liquid employing DFT calculations. J Mol Liq. 2016;222:796–803.
45. Ak F, Kebiroglu MH. Theoretical investigation of the chemical reactivity of acrylic acid molecules: a DFT study with UV-Vis, NMR, and FT-IR spectroscopy using STO-3G basis set. Yüzüncü Yıl Üniversitesi Fen Bilimleri Enstitüsü Dergisi. 2024;29(2):438–46.
46. Emami L, Faghih Z, Sakhteman A, Rezaei Z, Faghih Z, Salehi F, et al. Design, synthesis, molecular simulation, and biological activities of novel quinazolinone-pyrimidine hybrid derivatives as dipeptidyl peptidase-4 inhibitors and anticancer agents. New J Chem. 2020;44(45):19515–31.
47. Su S, Chen M, Li Q, Wang Y, Chen S, Sun N, et al. Novel penta-1, 4-diene-3-one derivatives containing quinazoline and oxime ether fragments: design, synthesis and bioactivity. Bioorg Med Chem. 2021;32: 115999.

48. Hashemi S, Jassbi AR, Erfani N, Kiani R, Seradj H. Two new cytotoxic ursane triterpenoids from the aerial parts of Salvia urmiensis Bunge. Fitoterapia. 2021;154: 105030.
49. Emami L, Khabnadideh S, Faghih Z, Farahvasi F, Zonobi F, Gheshlaghi SZ, et al. Synthesis, biological evaluation, and computational studies of some novel quinazoline derivatives as anticancer agents. BMC Chem. 2022;16(1):100.
50. Emami L, Faghih Z, Khabnadideh S, Rezaei Z, Sabet R, Harigh E, et al. 2-(Chloromethyl)-3-phenylquinazolin-4 (3H)-ones as potent anticancer agents; cytotoxicity, molecular docking and in silico studies. J Iran Chem Soc. 2021;18:1877–89.
51. Zhao C, Tang X, Chen X, Jiang Z. Multifaceted carbonized metal–organic frameworks synergize with immune checkpoint inhibitors for precision and augmented cuproptosis cancer therapy. ACS Nano. 2024;18(27):17852–68.
52. Humphrey W, Dalke A, Schulten K. VMD: visual molecular dynamics. J Mol Graph. 1996;14(1):33–8.
53. Fereidoonnezhad M, Faghih Z, Mojaddami A, Sakhteman A, Rezaei Z. A comparative docking studies of dichloroacetate analogues on four isozymes of pyruvate dehydrogenase kinase in humans. Dent. 2016;1(4):5.
54. Mojaddami A, Sakhteman A, Fereidoonnezhad M, Faghih Z, Najdian A, Khabnadideh S, et al. Binding mode of triazole derivatives as aromatase inhibitors based on docking, protein ligand interaction fingerprinting, and molecular dynamics simulation studies. Res Pharm Sci. 2017;12(1):21.
55. Morris GM, Huey R, Olson AJ. Using autodock for ligand-receptor docking. Curr Protocols Bioinform. 2008;24(1):8.14.1-8.40.
56. Rahmannejadi N, Khabnadideh S, Yavari I. Synthesis, docking, and cytotoxic activities of novel 2-aryl-4-(arylamino) quinazolines. Monatshefte für Chemie-Chem Mon. 2018;149(11):2085–92.
57. Li Z, Gu J, Zhuang H, Kang L, Zhao X, Guo Q. Adaptive molecular docking method based on information entropy genetic algorithm. Appl Soft Comput. 2015;26:299–302.
58. Baziar L, Emami L, Rezaei Z, Solhjoo A, Sakhteman A, Khabnadideh S. Design, synthesis, biological evaluation and computational studies of 4-Aminopiperidine-3, 4-dihyroquinazoline-2-uracil derivatives as promising antidiabetic agents. Sci Rep. 2024;14(1):26538.
59. Zhao Y, Truhlar DG. The M06 suite of density functionals for main group thermochemistry, thermochemical kinetics, noncovalent interactions, excited states, and transition elements: two new functionals and systematic testing of four M06-class functionals and 12 other functionals. Theoret Chem Acc. 2008;120:215–41.
60. Zhao Y, Truhlar DG. Density functionals with broad applicability in chemistry. Acc Chem Res. 2008;41(2):157–67.
61. Zhao Y, Schultz NE, Truhlar DG. Design of density functionals by combining the method of constraint satisfaction with parametrization for thermochemistry, thermochemical kinetics, and noncovalent interactions. J Chem Theory Comput. 2006;2(2):364–82.
62. Frisch M, Trucks G, Schlegel H, Scuseria G, Robb M, Cheeseman J, et al. Gaussian09 Revision D. 01. Wallingford: Gaussian Inc.; 2009.

Publisher's Note